AD-A204 895 DOWNSTREAM RAY TRACING IN BEAM OPTICS CODES(U) UTAH UNIV SALT LAKE CITY DEPT OF ELECTRICAL ENGINEERING W B REYES OCT 88 UTEC-MD-88-030 RADC-TR-88-210 1/1

UNCLASSIFIED F30602-84-C-0153 F/G 20/14 NL

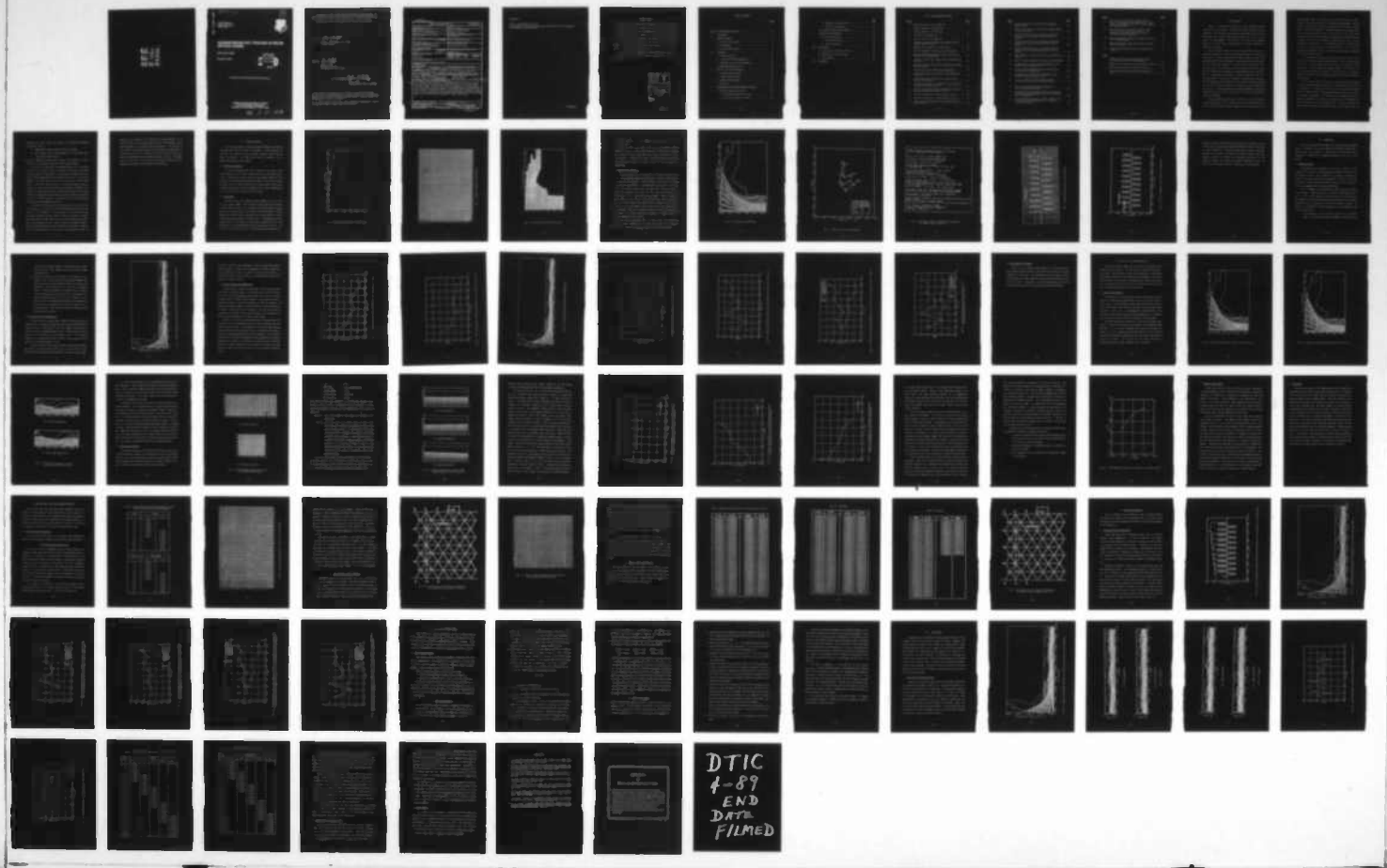


1·0
1·1
1·25
1·4
1·6
2·8
3·15
3·5
4·0
4·5
2·5
2·2
2·0
1·8

(4)

RADC-TR-88-210
Final Technical Report
October 1988

DOWNSTREAM RAY TRACING IN BEAM OPTICS CODES

University of Utah

Wilfredo B. Reyes

APPROVED FOR PUBLIC RELEASE; DISTRIBUTION UNLIMITED

ROME AIR DEVELOPMENT CENTER
Air Force Systems Command
Griffiss Air Force Base, NY 13441-5700

This report has been reviewed by the RADC Public Affairs Division (PA) and is releasable to the National Technical Information Service (NTIS). At NTIS it will be releasable to the general public, including foreign nations.

RADC-TR-88-210 has been reviewed and is approved for publication.

APPROVED: Andrew E Chrostowski

ANDREW E. CHROSTOWSKI, Capt, USAF
Project Engineer

APPROVED: Frank J Rehm

FRANK J. REHM
Technical Director
Directorate of Surveillance

FOR THE COMMANDER: John A. Ritz

JOHN A. RITZ
Directorate of Plans & Programs

If your address has changed or if you wish to be removed from the RADC mailing list, or if the addressee is no longer employed by your organization, please notify RADC (OCTP) Griffiss AFB NY 13441-5700. This will assist us in maintaining a current mailing list.

Do not return copies of this report unless contractual obligations or notices on a specific doucment require that it be returned.

UNCLASSIFIED

SECURITY CLASSIFICATION OF THIS PAGE

REPORT DOCUMENTATION PAGE

Form Approved OMB No. 0704-0188

1a. REPORT SECURITY CLASSIFICATION UNCLASSIFIED	1b. RESTRICTIVE MARKINGS N/A
2a. SECURITY CLASSIFICATION AUTHORITY N/A	3. DISTRIBUTION/AVAILABILITY OF REPORT Approved for public release; distribution unlimited.
2b. DECLASSIFICATION/DOWNGRADING SCHEDULE N/A	
4. PERFORMING ORGANIZATION REPORT NUMBER(S) UTEC MD-88-030	5. MONITORING ORGANIZATION REPORT NUMBER(S) RADC-TR-88-210
6a. NAME OF PERFORMING ORGANIZATION University of Utah 6b. OFFICE SYMBOL (If applicable)	7a. NAME OF MONITORING ORGANIZATION Rome Air Development Center (OCTP)
6c. ADDRESS (City, State, and ZIP Code) Department of Electrical Engineering 3280 Merrill Engineering Building Salt Lake City UT 84112	7b. ADDRESS (City, State, and ZIP Code) Griffiss AFB NY 13441-5700
8a. NAME OF FUNDING/SPONSORING ORGANIZATION AFOSR 8b. OFFICE SYMBOL (If applicable) NE	9. PROCUREMENT INSTRUMENT IDENTIFICATION NUMBER F30602-84-C-0153
8c. ADDRESS (City, State, and ZIP Code) Bolling AFB Wash DC 20332	10. SOURCE OF FUNDING NUMBERS PROGRAM ELEMENT NO. 61102F; PROJECT NO. 2305; TASK NO. J9; WORK UNIT ACCESSION NO. 17

11. TITLE (Include Security Classification)

DOWNSTREAM RAY TRACING IN BEAM OPTICS CODES

12. PERSONAL AUTHOR(S)

Wilfredo B. Reyes

13a. TYPE OF REPORT	13b. TIME COVERED	14. DATE OF REPORT (Year, Month, Day)	15. PAGE COUNT
Final	FROM Sep 84 TO Sep 87	October 1988	92

16. SUPPLEMENTARY NOTATION

This research was accomplished in conjunction with Air Force Thermionics Engineering Research Program (AFTER) AFTER-27. Wilfredo B. Reyes was an AFTER student from (over)

17. COSATI CODES		
FIELD	GROUP	SUB-GROUP
09	01	

18. SUBJECT TERMS (Continue on reverse if necessary and identify by block number)

PPM Focused Electron Beams; Beam Optics; Paraxial Based Codes; Simulation Codes; Periodic Permanent Magnet. (Old)

19. ABSTRACT (Continue on reverse if necessary and identify by block number)

Tunnel emittance growth in beams is a subtle phenomenon which requires the use of highly accurate simulation codes and methods to achieve reliable results. This report discusses use of self-consistent beam optics codes in studies of emittance growth in very long PPM focused electron beams. A novel method by which a given problem can be accurately solved in a stairstep series downstream is presented. The deformable mesh code ~~of Dr. Richard True~~ is used to simulate a gridded gun focused by a double period magnetic field used in a high power coupled cavity traveling-wave tube. Solution coupling across the boundary is presented in detail. The study also uncovered a fundamental problem with paraxial based codes (Neuman boundary implicit) making their use unsuitable in emittance growth studies.

Keywords:

20. DISTRIBUTION/AVAILABILITY OF ABSTRACT	21. ABSTRACT SECURITY CLASSIFICATION
☒ UNCLASSIFIED/UNLIMITED ☐ SAME AS RPT. ☐ DTIC USERS	UNCLASSIFIED
22a. NAME OF RESPONSIBLE INDIVIDUAL Andrew E. Chrostowski, Capt, USAF	22b. TELEPHONE (Include Area Code) (315) 330-4381
	22c. OFFICE SYMBOL RADC (OCTP)

DD Form 1473, JUN 86 *Previous editions are obsolete.* SECURITY CLASSIFICATION OF THIS PAGE

UNCLASSIFIED

Block 16. Supplementary Notes (Cont'd)

Litton Industries. This report was submitted in partial fulfillment of the requirements for the degree of Electrical Engineer.

ACKNOWLEDGMENT

I am indebted to the Air Force Thermionic Engineering and Research (AFTER) Program for its sponsorship of the work reported in this paper.

Research was conducted at the Electron Devices Division of Litton Industries. Appreciation is extended to: Mrs. Gwen Good for her help in the computer area, John Rominger for his assistance in the mechanical layout of the gun, Ron Herriott for the helpful discussions on the progress of the study, and John Oates, Glenn Schietrum, and Doug Kinnis for their assistance throughout the study.

I wish to thank Dr. Richard True for suggesting the project and providing unbounded assistance and guidance during the entire course of the study.

TABLE OF CONTENTS

LIST OF ILLUSTRATIONS AND TABLES

I. INTRODUCTION

Design of electron-beam systems in linear microwave devices involves three main elements: beam formation, beam focusing, and beam collection. The quality of the electron beam formed by the gun, the focusing system, and the collection system each play a major role in overall tube performance. The ability to put these three elements together and achieve high tube efficiency is of utmost importance in microwave tube design.

This ever present demand for higher tube efficiency has led to numerous developments in the areas of beam focusing and collection. Improvements in beam transmission have been realized through newly developed theories that established optimum entrance conditions necessary for proper beam focusing.[1,2] With the use of an electron optics code and electron beam analyzers, precise positioning of the beam minimum in the magnetic field region is accomplished with very high accuracy.[3,7] Developments in the area of beam collection have also contributed greatly in better tube efficiency. Ongoing work in beam collection design has led to a number of very efficient collection schemes that drastically reduce the power loss arising from heat dissipated in the collector. The most significant of these developments is multistage depressed collectors, which are reported to achieve efficiencies in excess of 80 percent.

These developments demonstrate the effects of proper beam coupling on tube performance. They also point out the fact that the majority of work in dc beam analysis has been concentrated in the collector and the

cathode-anode region. This brings out the tunnel region as another avenue in the continuous effort to improve tube performance. Articles written on beam behavior along the focusing structure stress its importance in spent beam analysis.[4] Accurate description of dc beam behavior along the focusing structure will not only result in vast improvements in spent beam models used in computer simulation of multistage depressed collectors, but will also drastically increase the accuracy of beam transmission predictions. It is therefore essential to include beam behavior in the tunnel region in any beam analysis. This is the motivating factor behind this study -- the need to investigate beam behavior along the focusing structure.

In the study of beam behavior along the length of the tube, a need arises for a means of measuring beam quality. In the accelerator community, this is accomplished through the concept of emittance or phase space area. Standard emittance, formally defined as the area of the beam phase space ellipse divided by π, has been used by accelerator physicists in their study of emittance growth found to occur in particle accelerators.

This concept has been carried over in the microwave tube industry through a similar parameter introduced by Dr. Richard True in his design of gridded guns.[6] He came up with a quantity called "tunnel emittance," which is essentially half the standard emittance normalized with respect to the beam tunnel radius. In his recent paper on tunnel emittance,[2] he used this parameter to intercouple problems generally encountered in electron beam systems of linear beam devices. Based on his observations that indicate occurrence of emittance growth in PPM focused TWT's, he

suggested that this growth could explain two phenomena frequently encountered in TWT's:

1. Degradation in beam transmission with tube length.
2. The increased rate of beam spreading of a dc beam after passing through a PPM structure.

His paper emphasized, among other things, the importance of tunnel emittance in the design and analysis of beam optical systems.

In order that occurrence of emittance growth could be properly verified, it is critical to have the ability to trace the electron beam from the cathode to the collector. In confined flow focused tubes, this could be easily accomplished by optic codes with the aid of a very large computer. The same could not be said in the case of PPM focused tubes. A stability problem arising in the solution process makes it necessary to break up the beam and solve the problem in segments. This segmentation process poses several problems with regards to the manner the beam is segmented and the boundary conditions that must be enforced to ensure a consistent solution. No criteria have yet been established with regard to this segmentation process.

Today there are several optics codes available that could be used in ray tracing. One such code is the deformable mesh electron optics code of Dr. True (DEMEOS).[3] It has found use in both electron gun and multistage depressed collector design. Numerical results of electron gun simulations using this code show very close agreement with experimental data obtained from the Litton electron-beam analyzer system.[4] Numerous computer simulations have been made with this code to trace the beam far downstream, but no known effort has been made to study the

accuracy of the results and to analyze the ray tracing method. It is imperative that the ray tracing method we use be very accurate, since tunnel emittance is an extremely sensitive parameter. It is the goal of this project to study and develop an accurate method of downstream ray tracing that will allow verification of tunnel emittance growth and enable dc beam analysis along the entire length of the tube. The DEMEOS electron optics code will be studied and modified to perform the beam segmentation necessary in PPM-focused tube simulations.

II. COMPUTER MODELING

This section presents the modeling process undertaken in using the deformable mesh electron optics code (DEMEOS). Brief discussions of each step are included to give the reader a general idea of how the model was obtained. The reader should refer to reference 3 for a detailed description of the process.

A. Electron Gun Selection

The need to experimentally verify results of this study places some restrictions on the choice of gun to be used in the computer simulation. The gun must provide a small and very laminar beam to be able to achieve the highest beam transmission possible. The choice of design is also limited to Litton production guns to assure parts availability, minimize design time, and lower production cost. These considerations led to the choice of the L5637 gun for this study.

B. Gun Modeling

The first step in gun modeling using the DEMEOS code is to trace out the logical diagram. This involves outlining the gun's boundary contours (shown in Fig. 1) in a regular mesh denoted "logical" space. Each of the corner points in the logical space corresponds to a real geometrical position and are associated with a given potential. Figure 2 shows the logical diagram for the L5637 gun. Transformation from this logical space to real space is automatically accomplished by the code resulting in an irregular-triangle relaxation mesh shown in Fig. 3. It is on this relaxation mesh that the finite-difference approximation of

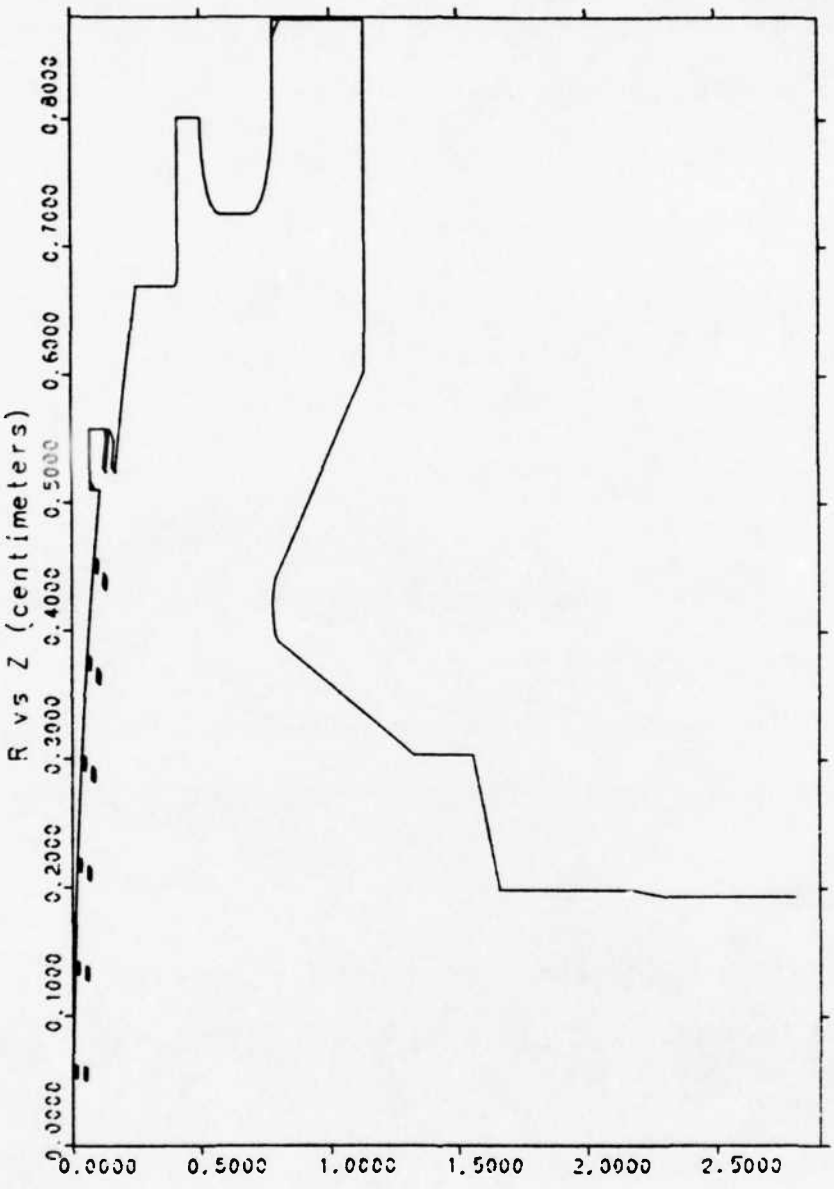

Fig. 1. Electrode contours for the L5637 gun.

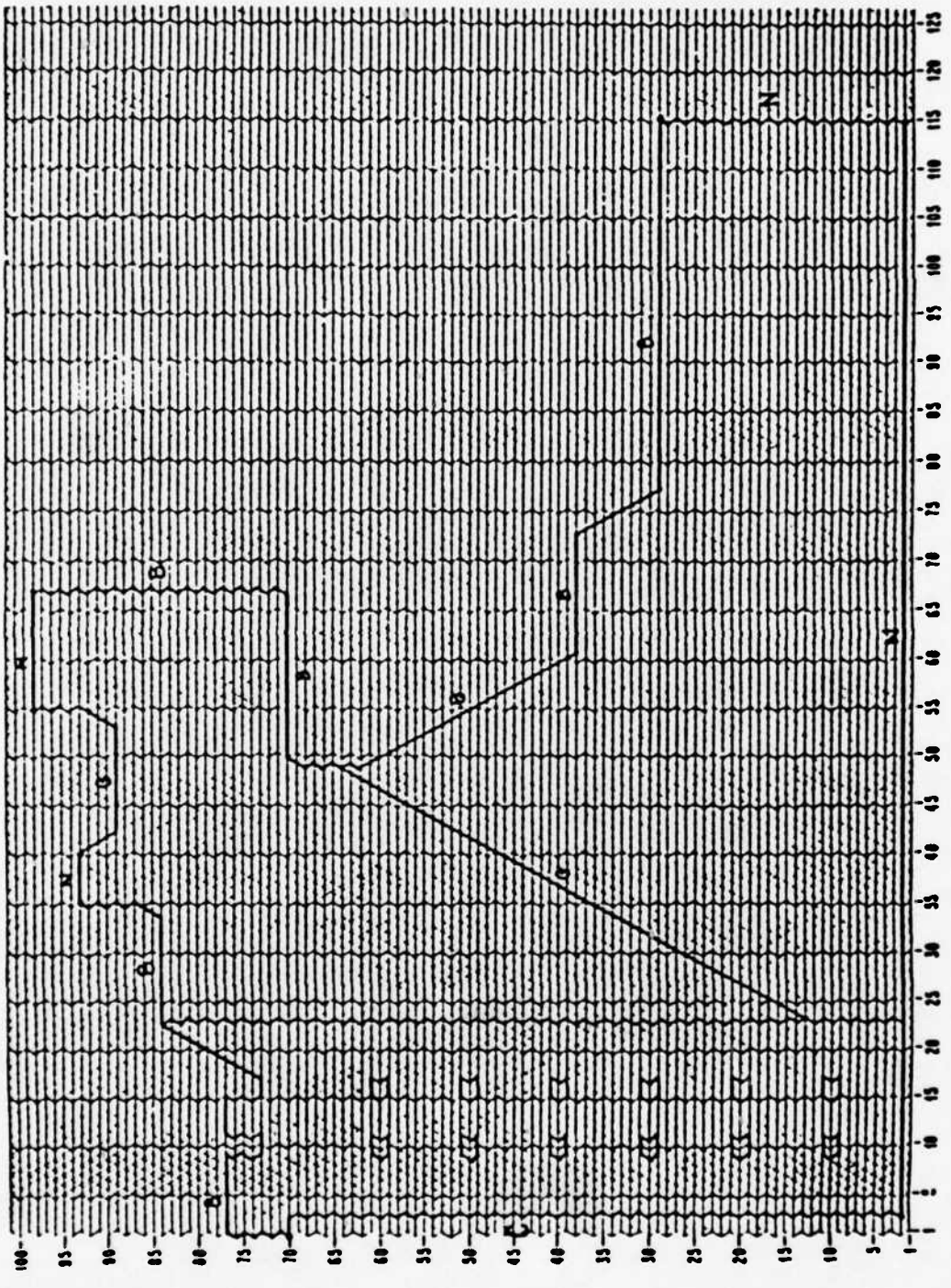

Fig. 2. Logical diagram for the L5637 gun.

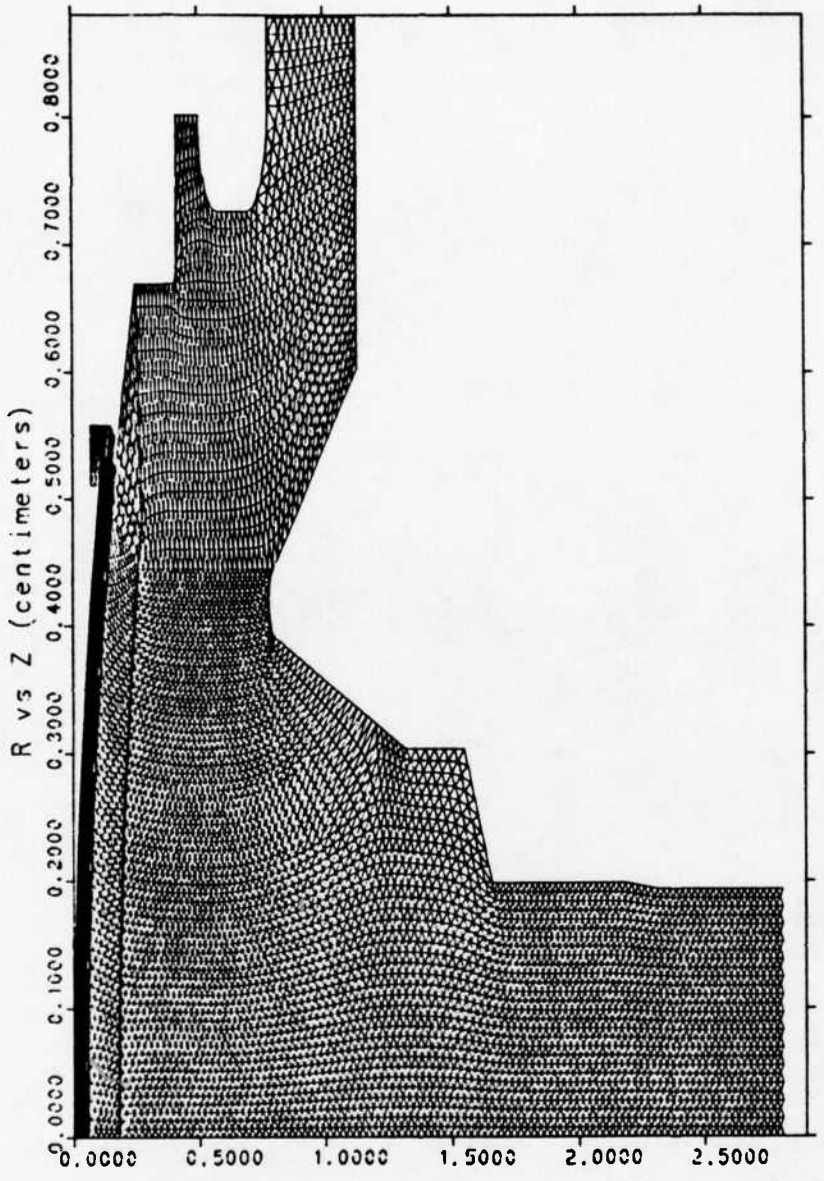

Fig. 3. Relaxation mesh for the L5637 gun.

Poisson's equation is solved. Figure 4 shows the solution for this particular gun.

Once the model of the gun is set up in the computer, several simulation runs at various cathode-to-anode distances with different grid voltages are made. From these runs, hairpin curves shown in Fig. 5 are obtained. Through these curves, the optimum operating perveance, cathode-to-anode distance, and grid voltage for the gun design are determined.[5]

C. Electron Beam Focusing

This gun design must now be matched to a suitable focusing structure. The appropriate magnetic field needed to focus the beam formed by this gun must be determined. The peak magnetic field value is obtained using True's code GUNPPMC, a PC program based on his work.[6] The printout of the output, shown in Fig. 6, shows that 1.425 kG rms will be sufficient to properly focus this beam. This leads to the choice of the L5638 tube body for this particular gun design. Figure 7 shows the axial magnetic field profile of the L5638 showing a peak value of 2.8 kG. The values used in the simulation were obtained from the actual values of the L5638 magnetic field scaled to get the desired peak B-field values. The first single-peak field was adjusted and positioned according to the method described in reference 1. Figure 8 shows the resulting magnetic field profile.

Note that the nonthermal model was used in all of the simulations in this study. Simulations were made using thermal and nonthermal models to determine the agreement between the resulting solutions. The

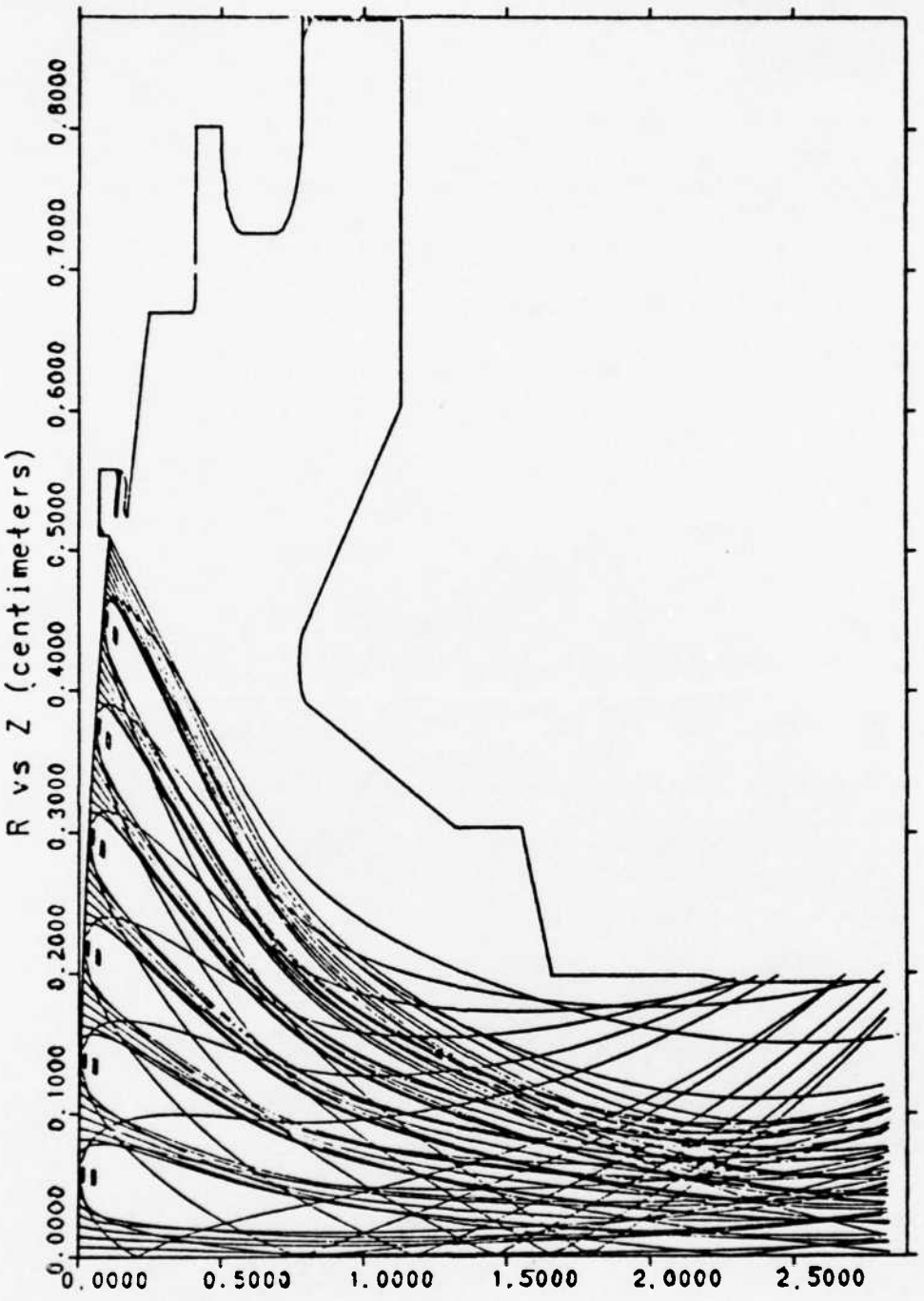

Fig. 4. Solution for the L5637 gun.

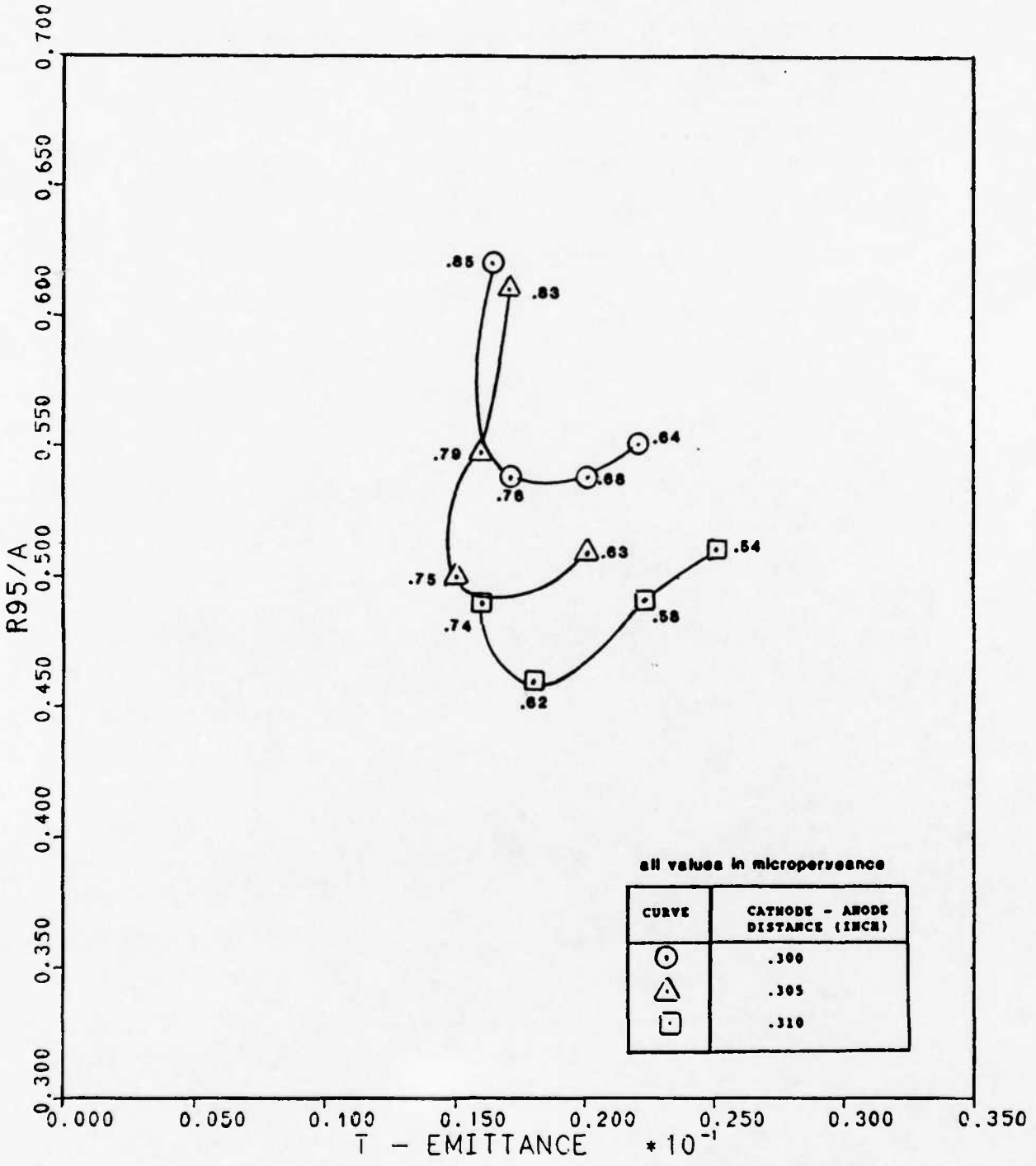

Fig. 5. Hairpin curves for the L5637 gun.

```
GUNPPMC (GUNPPMX): Program after Trans. E.D. 1984, 1987
Vers. 1.3, VAX, Basic, R. True, 10-23-87


Units: enter 1 for cm, 2.54 for inches? 2.54

Case Name =? L-5637 GUN FOR RAY TRACING STUDY

enter disk rc, V0 (kv), pmu? .2,26,.7548

enter r95/a, a (ckt i.r.), period L
(note: pulse r95/a = .6 opt, .65 mx; cw .45 opt, .5 mx)
? .5463,.076,.524

i0 = 3.1644     rb= .415188E-01     rc/r95 = 4.81709
calc th = 24.5979 deg
enter actual th or 0 to bypass? 24.2
actual th = 24.2 deg    delta th = .397911 deg

cath sph rad = .487896     cath area = .847993 cm^2

ungr: j0 = 3.4037     ja = 3.73164     je = 4.09117 a/cm^2
beam j = 90.5701 a/cm^2
enter scrn factor (diode=0, sh.g.=.17 (typ), i.g=.1 (typ))? .17
enter cath usage factor (sh.g.=.7 (typ), i.g. and u.l.t.=1 (typ),
c.g.=.85 (typ))? .7
gr: j0 = 5.85835     ja = 6.42279     je = 7.0416 a/cm^2

calc sigma = .0363 (note: calc sigma from actual th if entered)
enter actual sigma (e.g. from analyzer) or 0 to bypass? .033264

enter T(deg C) to calc thermal sigma or 0 to bypass? 1130
thermal sigma = .734543E-02

enter factor F (1.65 default) (note: for axial CCTWT B vals use F=1.3)? 1.3
B+/Bbr = 1.29482
Bbr = 1.10059     B+(rms) = 1.42507 kgauss
B+ pk s.p. = 2.01535     B+ pk d.p. = 2.37512 (note: B+ pk d.p.=B+(rms)/.6)

focfl = 2.37017     lamda_p/L = 3.29157
(note: pulse lamda_p/L>2.7 and cw lamda_p/L>3.2)
Vs.b.(kv) = 3.04469     Vs.b./V0 = .117104
T-emittance = .181721E-01
```

Fig. 6. Printout of output of GUNPPMC using parameters from DEMEOS thermal insulation.

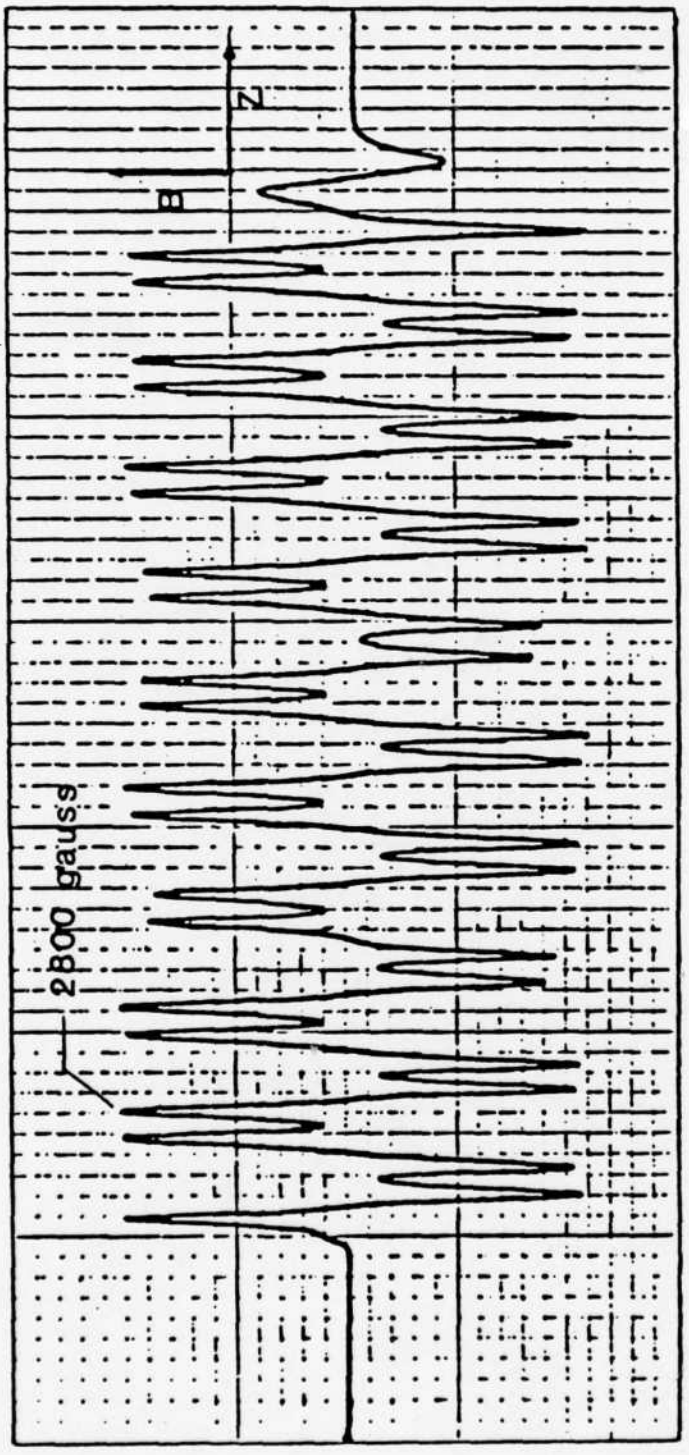

Fig. 7. Magnetic field profile of the L5638 tube

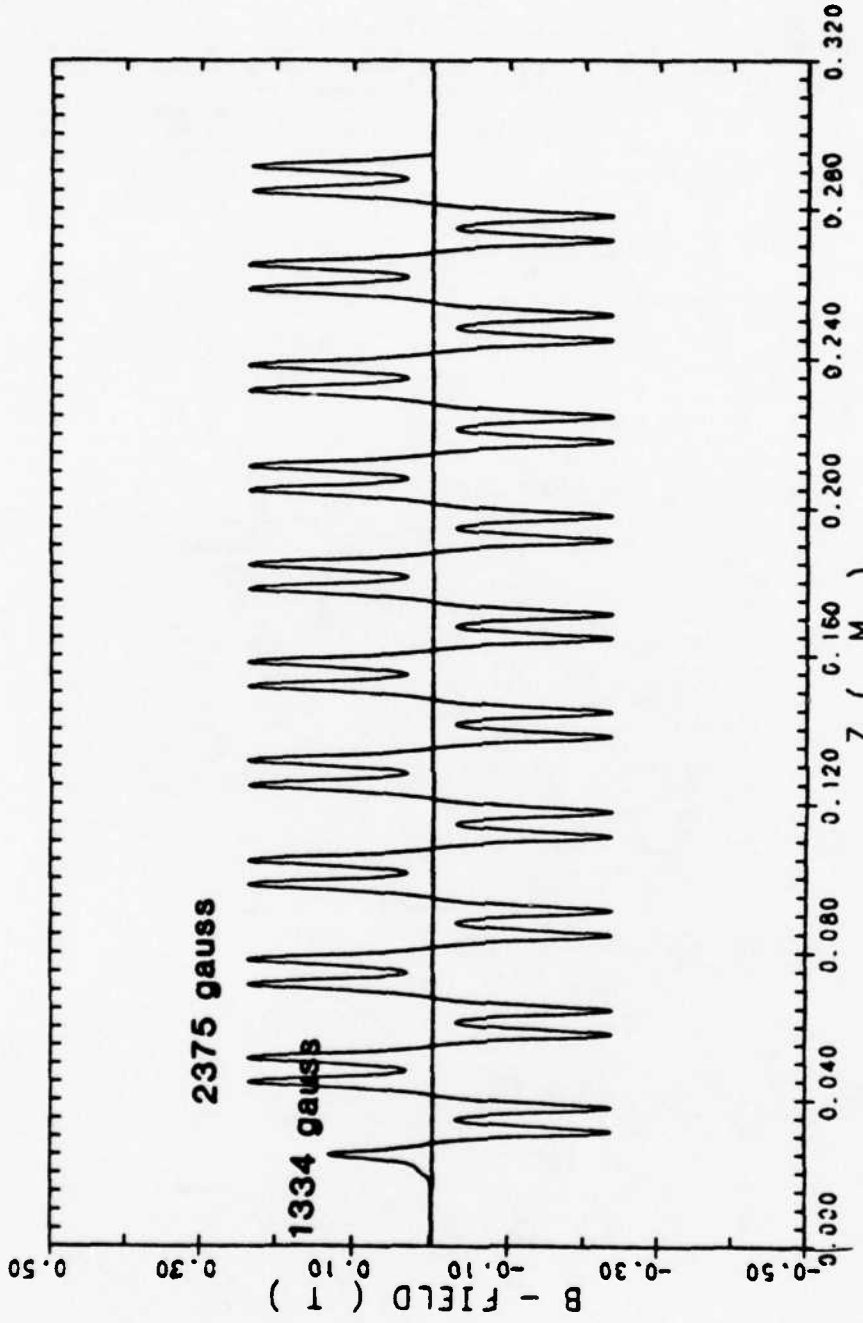

Fig. 8. Profile of magnetic field used in the simulations

nonthermal models yielded beam filling factors and t-emittance values that were very close to those obtained using thermal models. The effect of thermal velocities in these emittance growth studies are minimal compared to the effects of the grid on the value of sigma. This close agreement between the thermal and nonthermal simulations and the increased computer time involved in thermal simulations led to the choice of the nonthermal model as the vehicle in our investigation.

III. SIMULATION

This section discusses the process of ray tracing using the DEMEOS code. It describes the current method of simulating dc beam behavior from the gun to the collector. A simulation of a PPM focused tube is presented to demonstrate the problems encountered in the use of this method.

A. DEMEOS Simulation

As mentioned before, simulation of the entire region of a PPM focused tube could not be performed without encountering instability in the solution process. This instability is avoided by limiting the length of the region included in the simulation. This led to the present method of dividing the entire region, from the cathode to the collector, into segments and solving them separately.

The first segment in the simulation includes the gun and a portion of the tunnel. Poisson's equation is solved in this region, and ray data at the end of the tunnel are saved and used in the next region. The segments following the gun region are continuations of the tunnel. Continuation runs are made until the collector region is reached. The length of the segments in these continuation runs is dictated by the following restrictions:

1. The length must be such that the solution will be convergent. It is desirable to make the segment as long as possible

to speed up the solution process. On the other hand, increasing the length of the segment will require a much longer convergence time.

2. Simulation runs must end and begin at the location of zero magnetic field. This restriction arises because DEMEOS does not take into account any rotational motion of the beam at the beginning of each simulation run. This was a deliberate effort to avoid the additional complexity that the beam's rotational motion will bring to the code. Knowing that the beam's rotational motion is zero at the location of zero magnetic field, the beginning and ending of any simulation at the location of zero magnetic field justifies neglect of this rotational motion. This limitation does not in any way affect the accuracy of the result.

B. Simulation with Beam Segmentation

A simulation run using the present segmentation method (with more segments than is customary) was made and the resulting beam profile is shown in Fig. 9. The length of the first segment was adjusted to include the first single-peak magnetic field. Termination was made to coincide with the location of zero magnetic field. The succeeding segments or continuation runs were all made to each include one full period of the double-peak magnetic field.

The beam profile of Fig. 9 shows an electron beam that is getting more laminar as it moves away from the cathode. The plots of the tunnel emittance and beam radius along the length of the tunnel, shown in Figs.

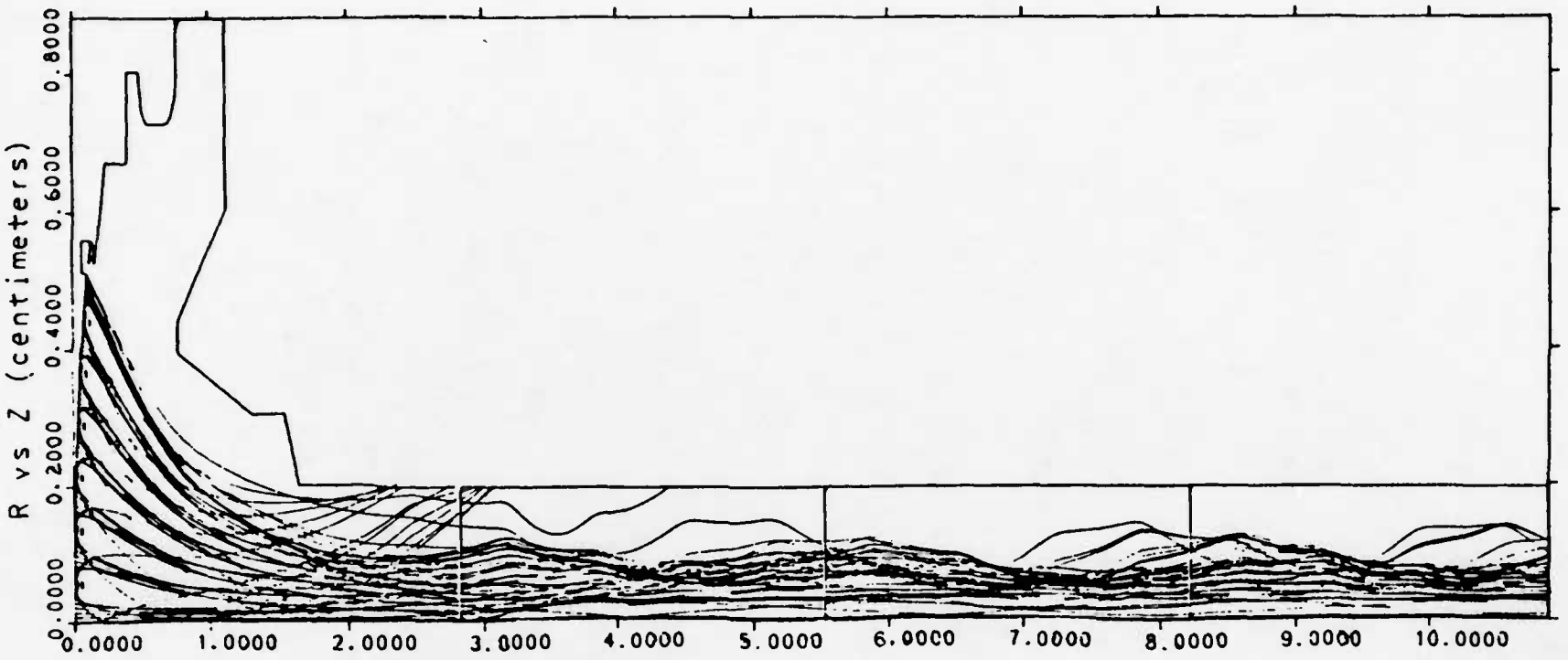

Fig. 9. Electron trajectories using the present ray tracing method with beam segmentation.

10 and 11, show the beam decreasing in size and exhibiting negative emittance growth. The electrons are behaving as if they are experiencing a cooling down process as they flow away from the cathode. To verify the validity of this solution, a second simulation run was performed in a different fashion.

C. Simulation without Beam Segmentation

As noted before, no work has been made to verify the accuracy of the present ray tracing method. On the other hand, results of simulation runs without beam segmentation have been verified to be accurate through the use of electron beam analyzers. This provided a means by which the solution of the first simulation run could be verified. By simulating the entire length of the first simulation without breaking up the beam, a reliable solution is obtained. To avoid the problem of instability, the length of the region included in the simulation was adjusted until convergence of the solution was reached.

Figures 12, 13, and 14 show the beam profile resulting from this simulation and the corresponding plots of tunnel emittance and beam radius along the tunnel. The figures show an electron beam behaving completely different from the beam of Fig. 9. The beam is very nonlaminar and the smoothing observed before has disappeared. The difference between the two solutions is emphasized by superimposing the curves as shown in Figs. 15 and 16. Since solutions of other beam optics problems obtained in a similar process have been proven to be accurate, the beam profile of Fig. 12 is the true picture of electron behavior inside the tunnel.

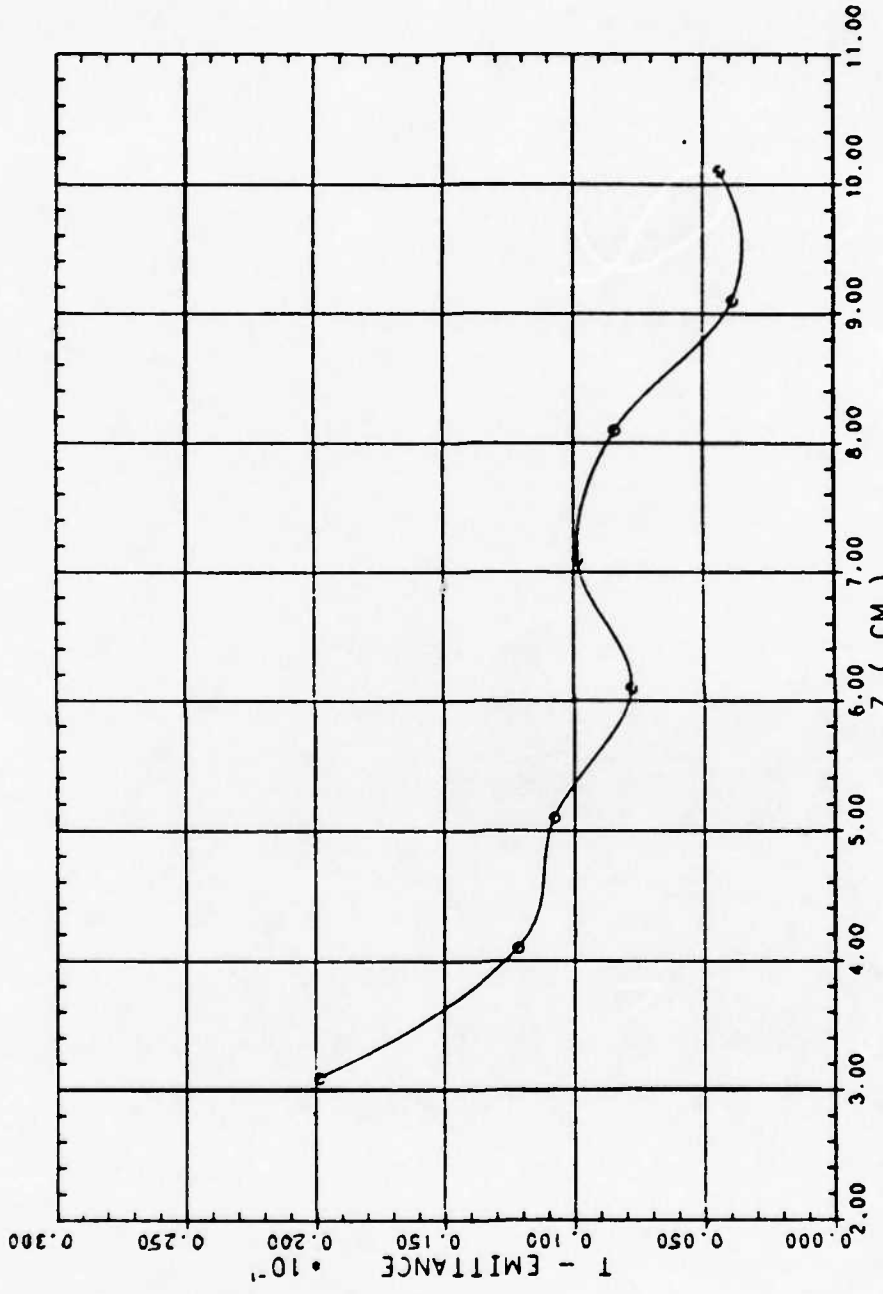

Fig. 10. T-emittance versus axial distance for the beam profile of Fig. 9.

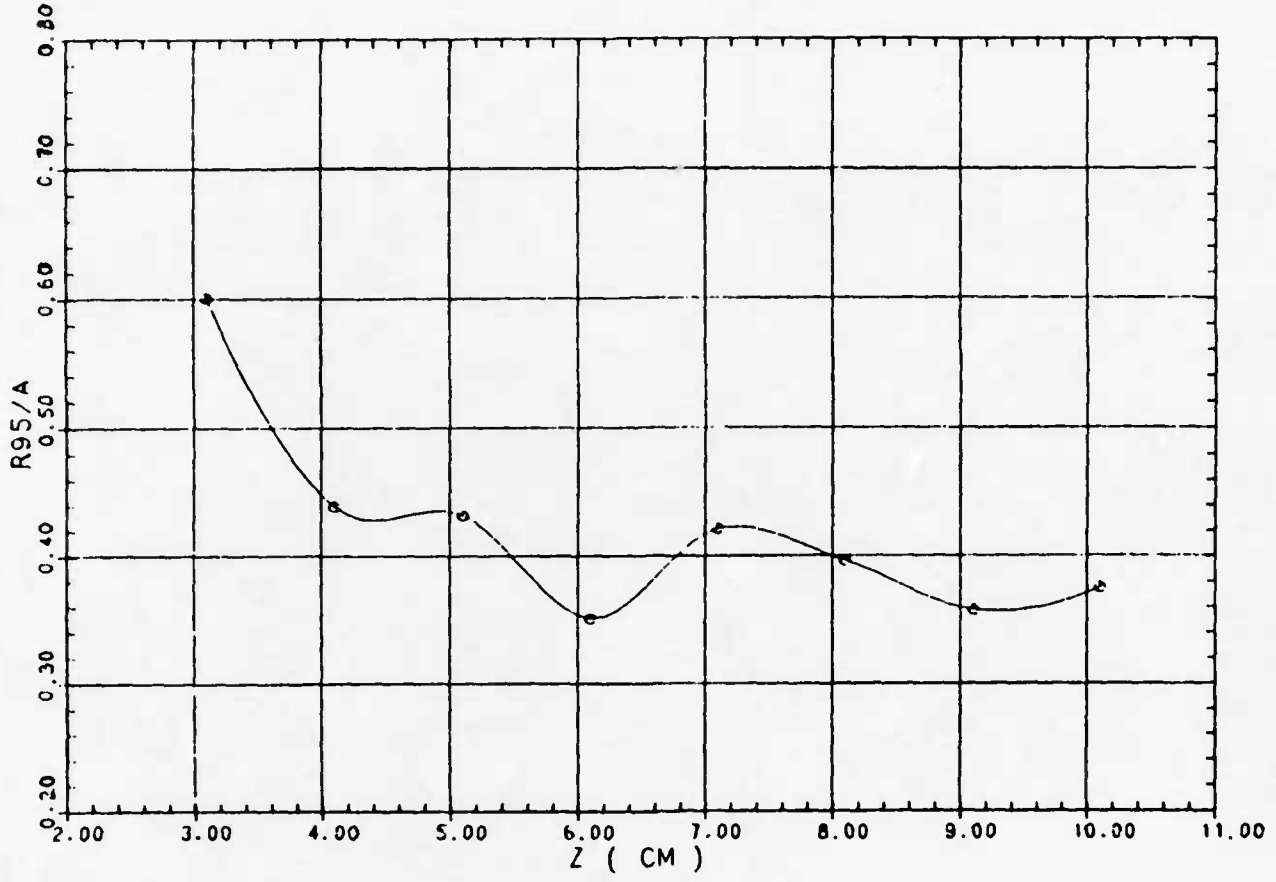

Fig. 11. Beam filling factor versus axial distance for the beam profile of Fig. 9.

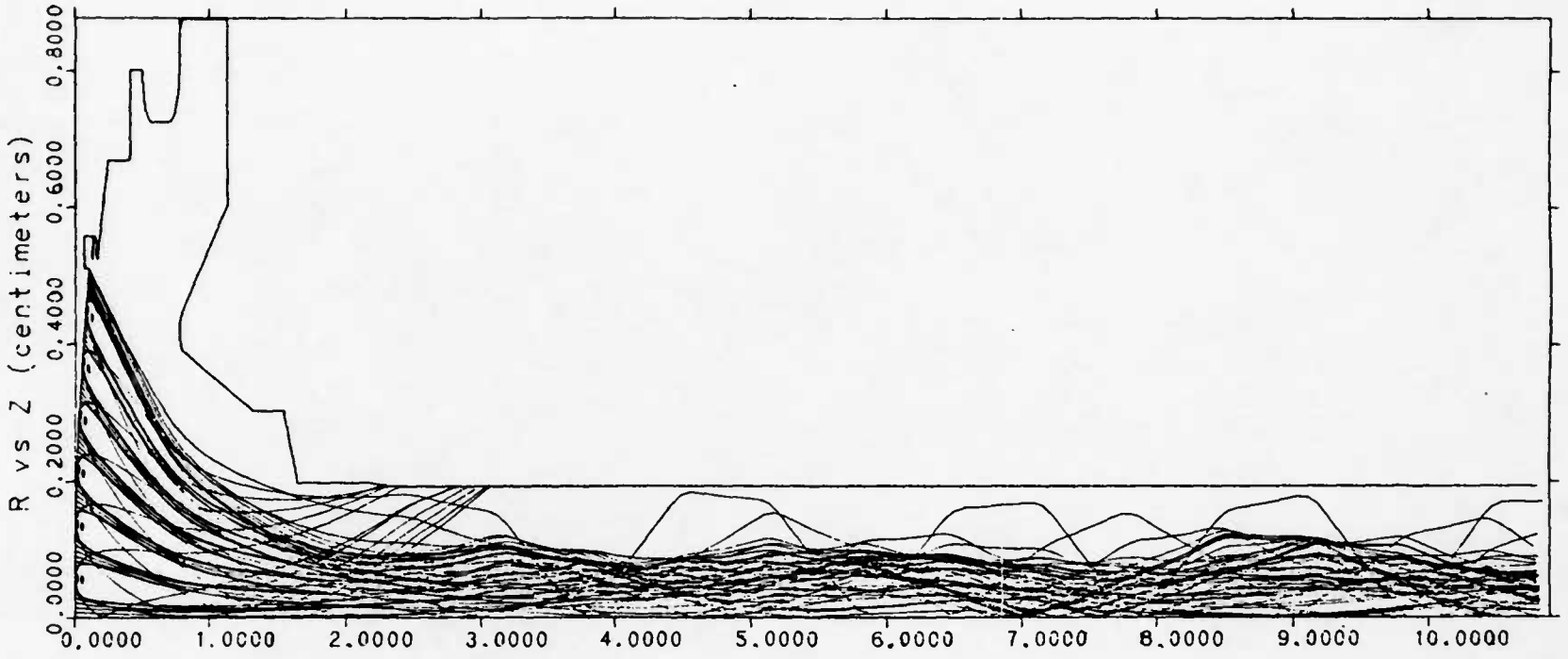

Fig. 12. Electron trajectories without beam segmentation.

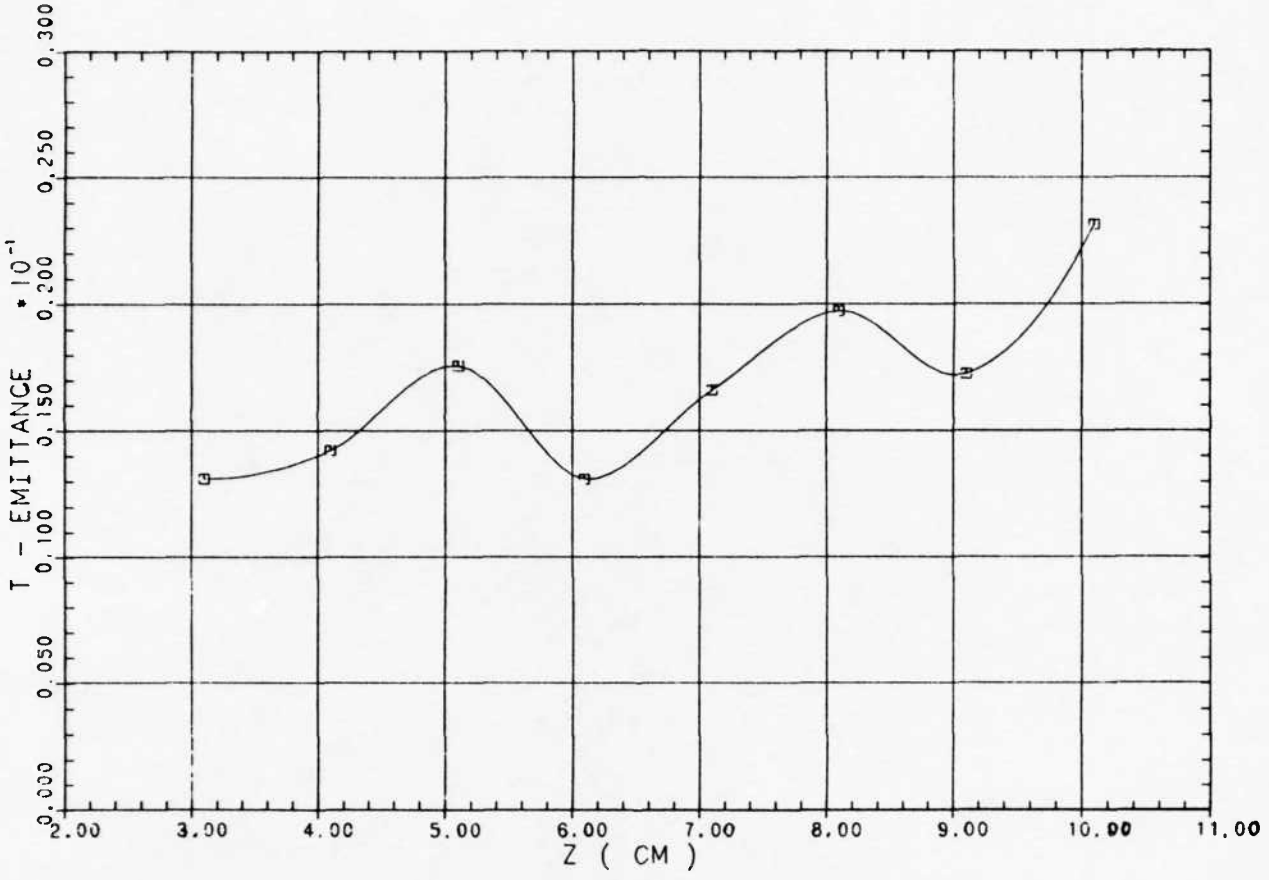

Fig. 13. T-emittance versus axial distance of the beam profile of Fig. 12.

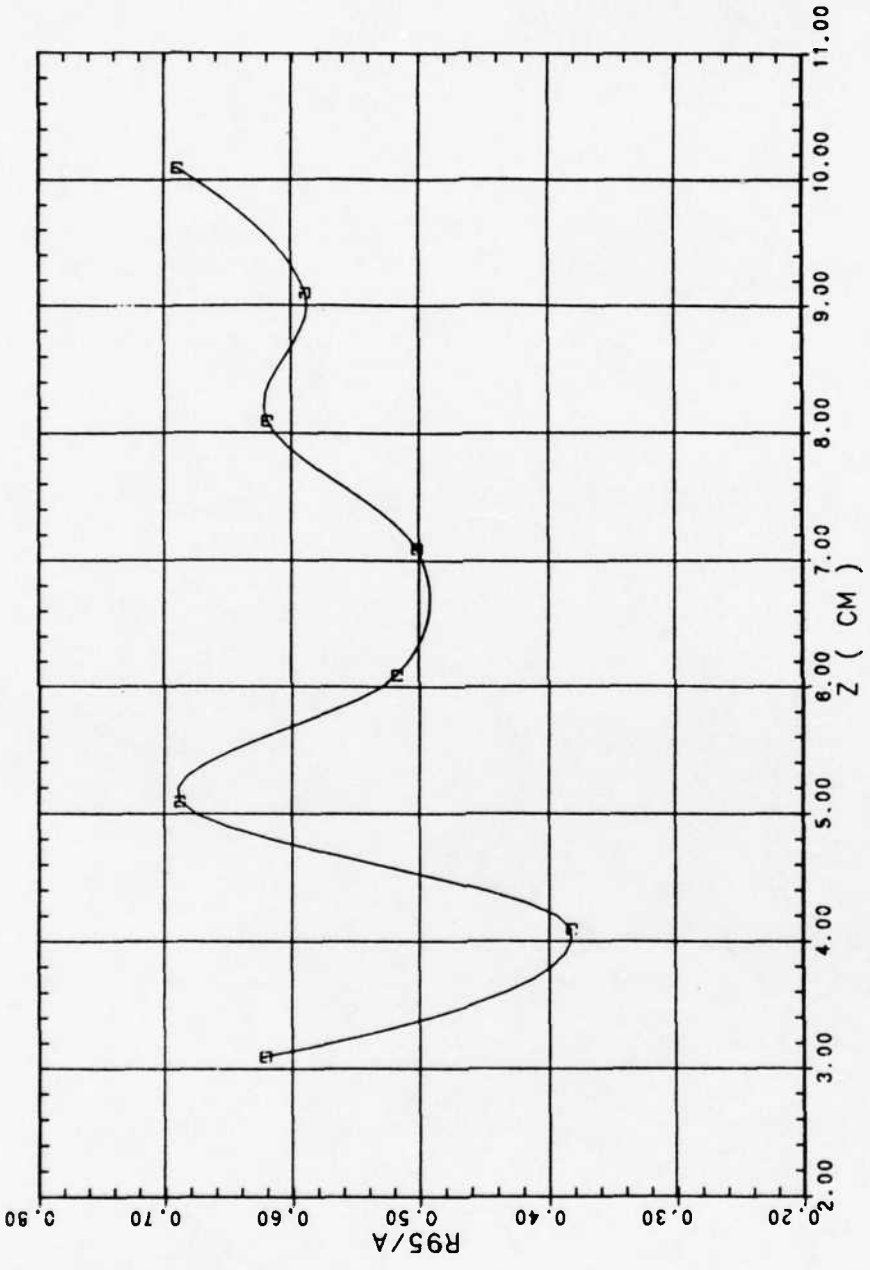

Fig. 14. Beam filling factor versus axial distance for the beam profile of Fig. 12.

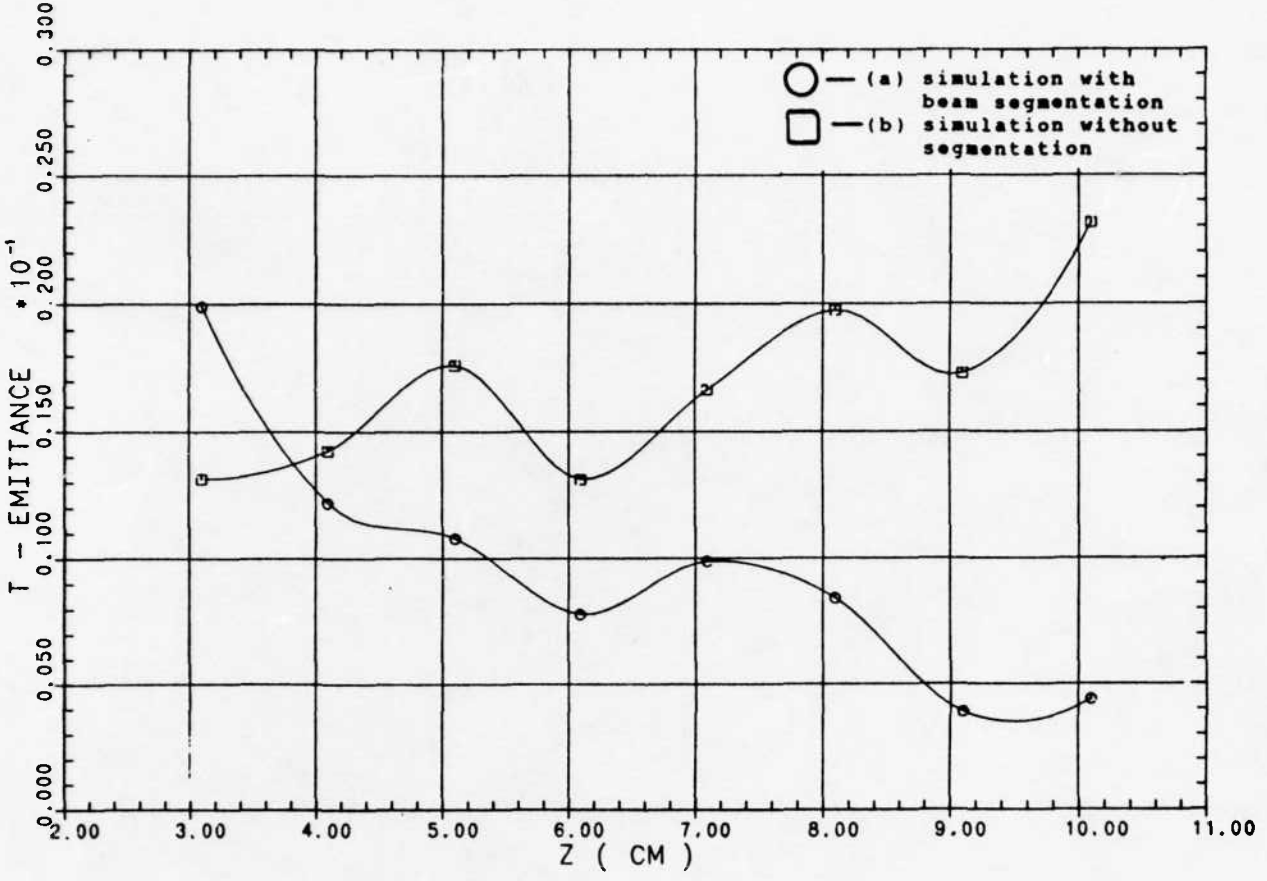

Fig. 15. T-emittance versus axial distance for the two electron trajectories of Figs. 9 and 12.

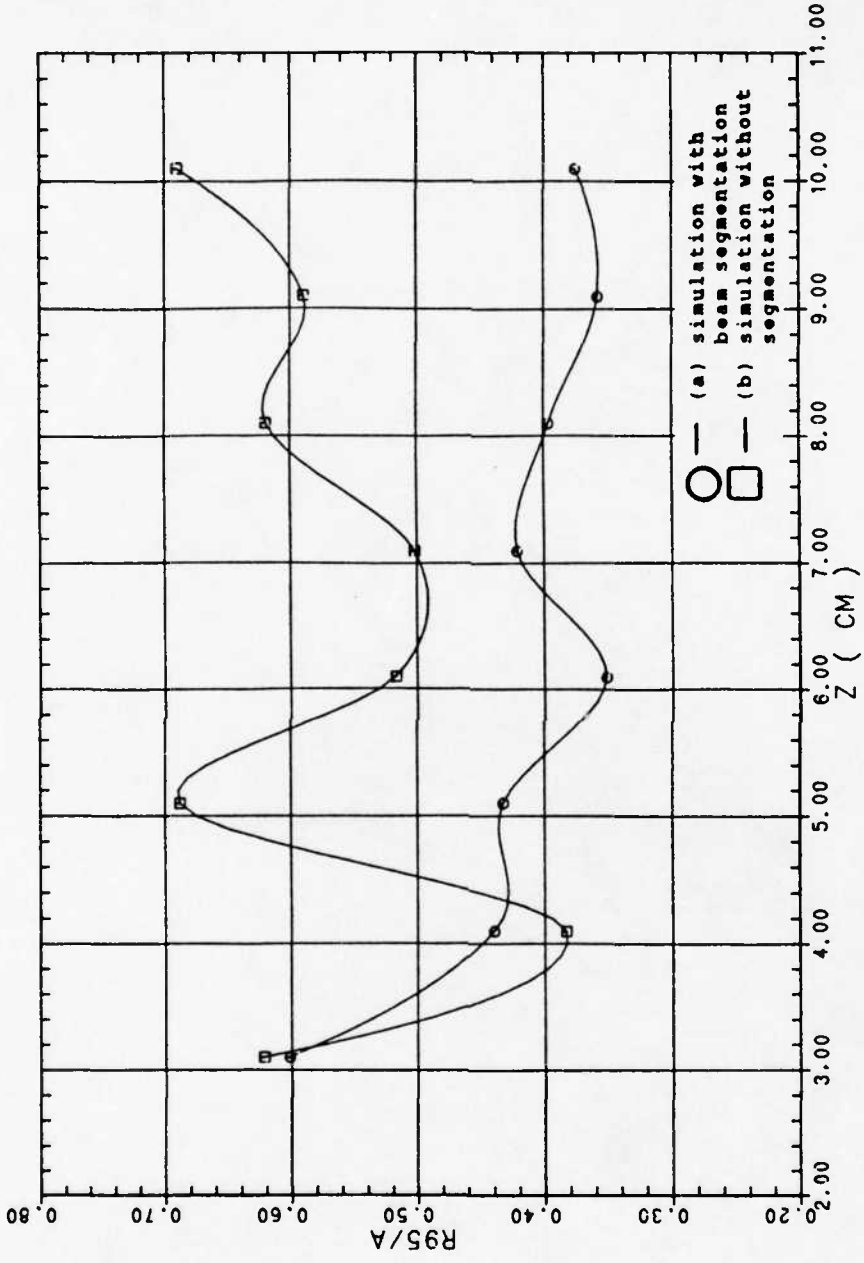

Fig. 16. Beam filling factor versus axial distance for the two electron trajectories of Figs. 9 and 12.

D. Beam Segmentation Problem

These two very different beam profiles for the same electron optics problem clearly manifest the existence of a problem in the present method of ray tracing. This demonstrates that the process of splitting the region into small segments and solving them individually is not a trivial process. Guidelines on proper beam segmentation need to be established to make this ray tracing method accurate and reliable.

IV. STUDY OF THE RAY TRACING METHOD

The previous section pointed out the presence of a problem in the present ray tracing method. The next task is to determine the cause of the problem. This section will deal with these matters. The present ray tracing method will be investigated and the parameters in the simulation process will be studied to determine their effects on the solution. Possible sources of error will be discussed, and the role they play in altering the solution will be pointed out.

A. Boundary Specifications

Determination of the approximate area where the problem initially surfaced is accomplished through careful study of the beam profiles of Figs. 9 and 12. Close examination reveals the profiles almost identical in the first region, but very much different in the following region (see Figs. 17, 18, and 19). This suggests that the problem lies in the extraction and injection of ray data from one simulation run to another. Focus of attention could therefore be directed to these processes.

One factor that plays a major role in the solution process, especially in the ray data extraction and injection, is the boundary specifications. It is at the boundaries that rays are extracted and injected. It is also through the conditions specified at the boundaries that the finite-difference approximations of the Laplace's and Poisson's equations are solved. It is crucial that the proper boundaries be correctly specified to ensure consistency in the solution.

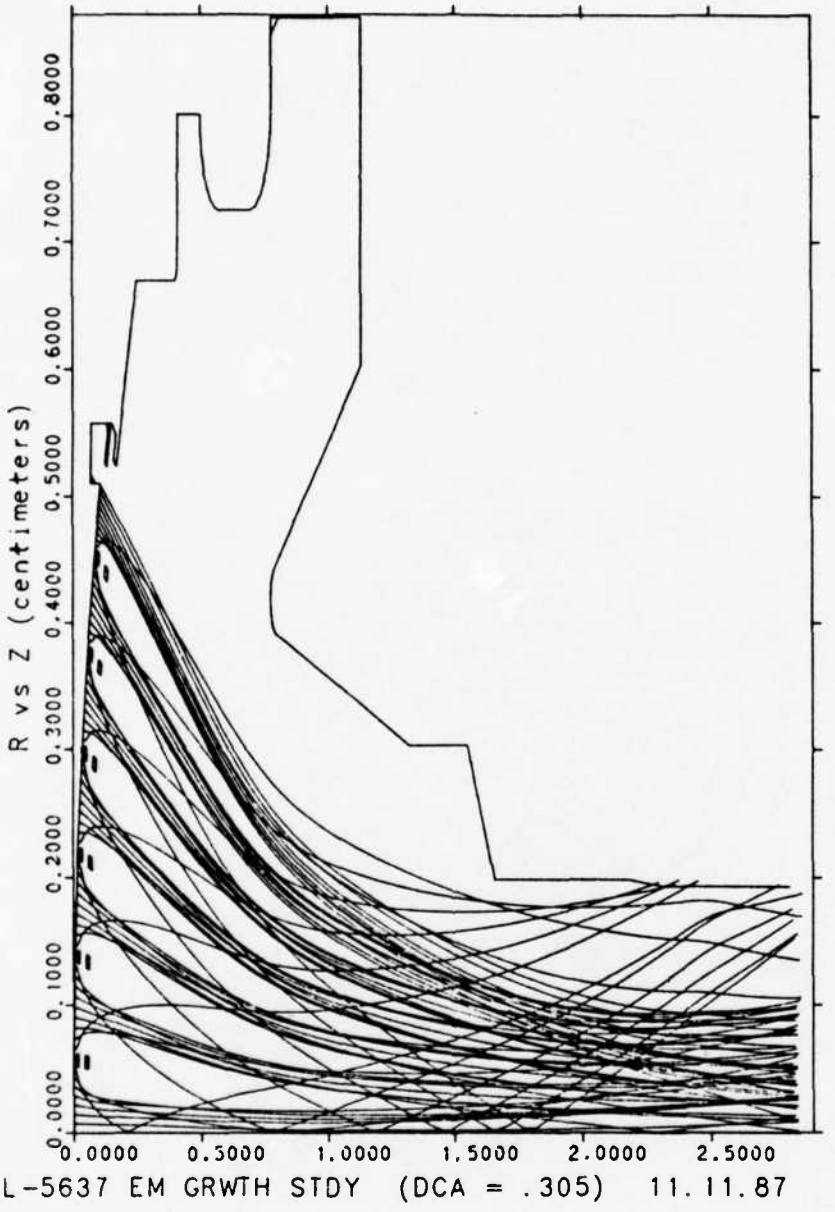

Fig. 17. Electron trajectories in the gun region of Fig. 9.

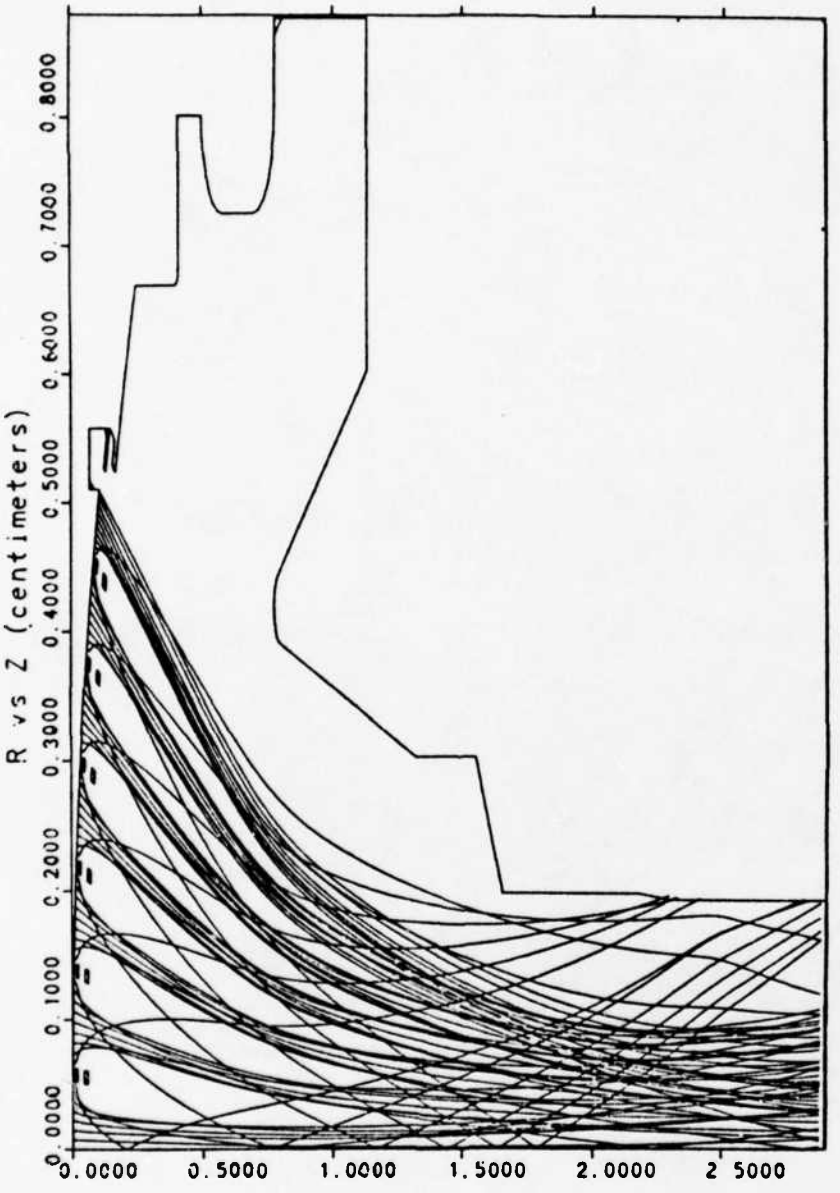

Fig. 18. Electron trajectories in the gun region of Fig. 12.

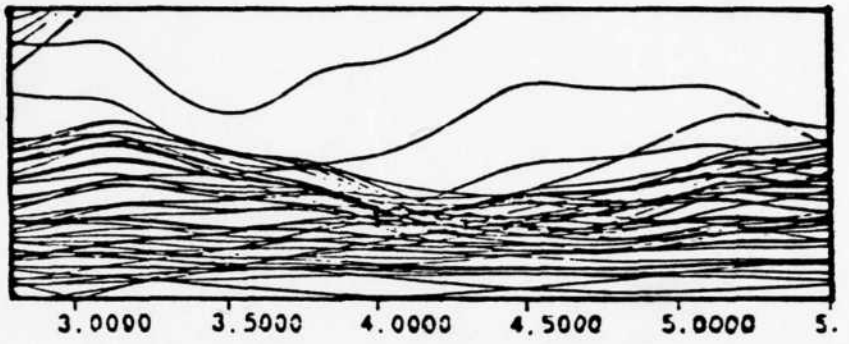

(a) With beam segmentation.

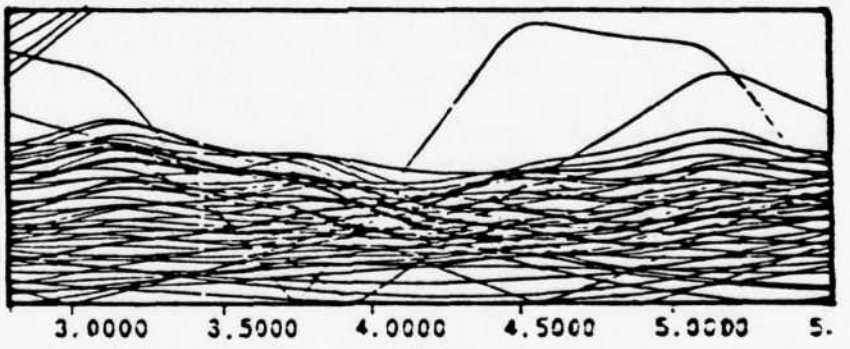

(b) Without beam segmentation.

Fig. 19. Flow pattern downstream of the two simulation runs of Figs. 9 and 12.

The three main boundaries used in the DEMEOS code are the B, C, and N boundaries. These boundaries are shown on the logical diagram of Fig. 2. The C boundary, normally associated with the cathode surface, is not of interest to us in this study, since it is not involved in data extraction or injection. The B and N, however, are the major boundaries involved in the segmentation process.

B boundaries are boundaries that apply to regions associated with fixed potentials. It is synonymous with the Dirichlet boundary wherein the potential function is known on the boundary surface. Examples of this boundary are the focus electrode contour, the anode, and the tunnel wall. N or Neuman boundaries, on the other hand, apply to regions where the normal derivative of the potential function is known. They are shown on the logical diagram defining regions where symmetry is assumed to exist. Since the normal derivative is also an unknown in the problem, DEMEOS uses the special case of the Neuman boundary condition, i.e., the normal derivataive of the potential function is set to zero. This in effect forces the potential to remain constant across the boundary. This plays a very significant role in the solution process.

B. Neuman Boundary Effects

To determine the extent of the effect of this artificial condition enforced across the boundary, a study was made in which a very laminar beam with a uniform current density profile was injected inside a tunnel whose boundaries are defined according to the logical diagram of Fig. 20a. Simulation was made under the following conditions:

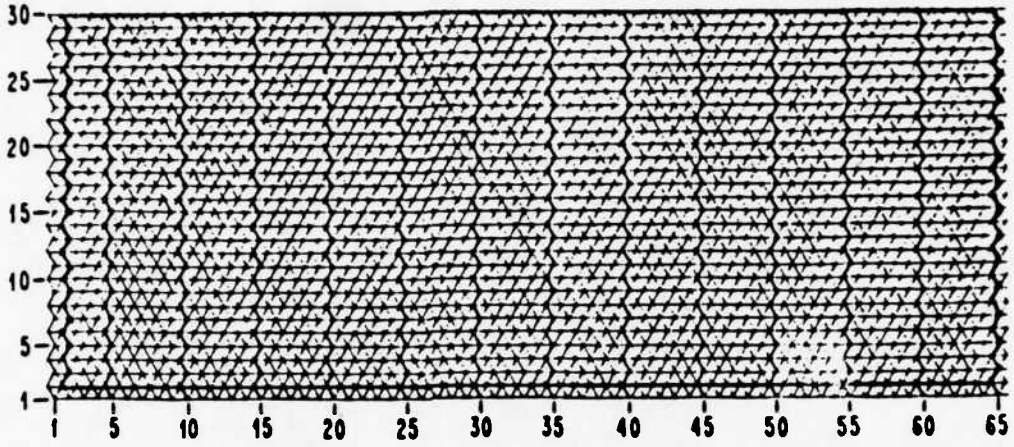

(a) Tunnel for Case I.

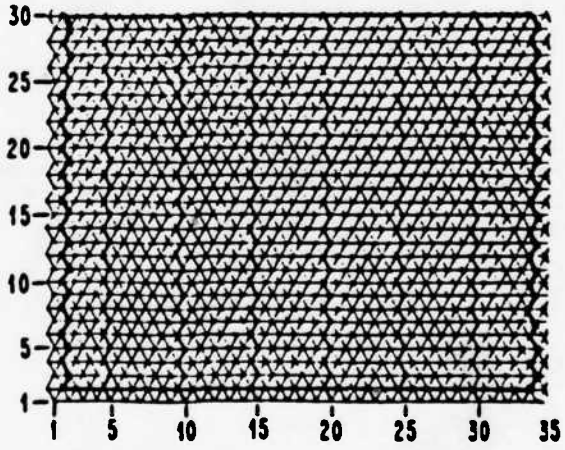

(b) Tunnel for Case II.

Fig. 20. Logical diagram of the tunnel used in the Neuman boundary study

Vo	26 kV
Perveance	0.755 microperveance
Tunnel length	1 cm
Tunnel radius	0.16428 cm
B-field start	10 kG

The beam trajectory was controlled by varying the magnetic field linearly along the tunnel. The magnetic field was adjusted to obtain beams with negataive, positive, and zero trajectories. Two cases were simulated:

Case I The entire length of the tunnel was included in the simulation.

Case II Only one half of the tunnel region of Case I was included. The boundaries were defined according to the logical diagram of Fig. 20b. All parameters were kept the same as Case I, except for the length of the region included in the simulation. This change was made to determine the effect of a Neuman boundary in the middle section (z = 0.5 cm) of the region of Case I. Any difference between the solution of this case and the solution of Case I could be attributed solely to this Neuman boundary.

Figure 21 shows the beam profiles resulting from the simulation of the entire tunnel. It is noteworthy to mention that each of these profiles resulted in a unique potential distribution. Comparison of the solutions of the two cases is made by plotting the potentials at a

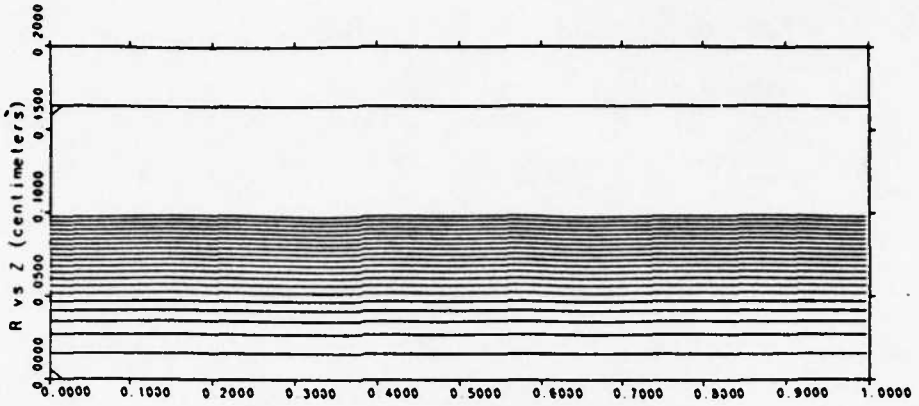

(a) Zero trajectory.

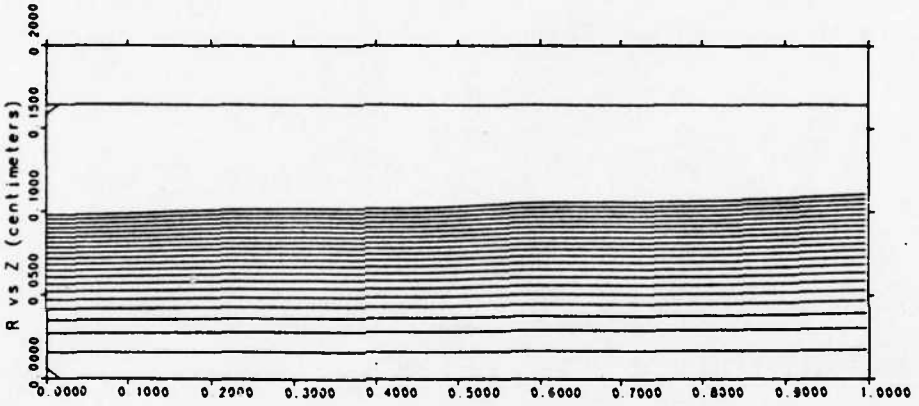

(b) Positive trajectory.

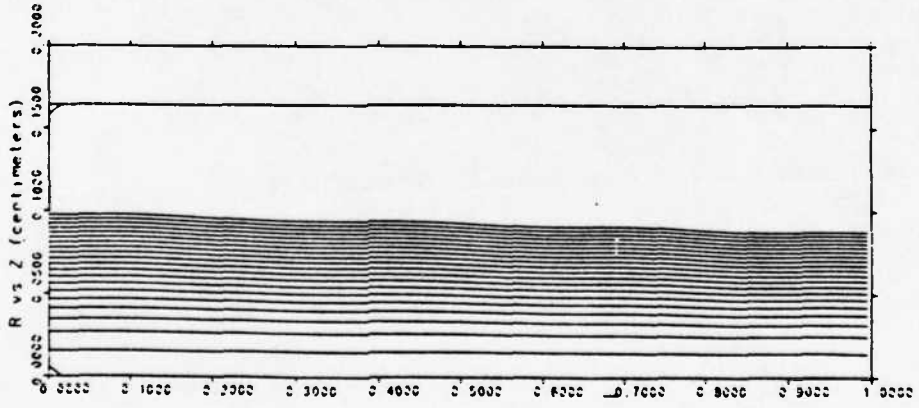

(c) Negative trajectory.

Fig. 21. Electron trajectories of laminar beam launched inside the tunnel of Fig. 20.

constant radius along the tunnel region. Figures 20, 21, and 22 show the plots of these potentials for the three potential gradients.

The solid curve of Fig. 22 is a portion of the potential distribution at a constant radius along the tunnel of Case I. It shows the potential remaining constant at a radius of $r = 0.1466$ cm along the tunnel. The dashed curve, shown coincidental with the solid curve, represents the potential distribution at the same radius along the tunnel of Case II. The agreement between these two solutions demonstrates that insertion of the Neuman boundary at $z = 0.5$ cm did not change the solution. This is as expected, since the condition that Neuman boundary enforces in Case II happens to be the condition occurring at that location in Case I. Case II is just a simulation of the first half of Case I. We could therefore conclude that the solution is not affected by the special Neuman condition in cases where the potential distribution is constant across the boundary. Figure 23 shows the case where the potential is increasing along the tunnel. The two curves are coincidental only at regions away from the boundary. They begin to deviate from each other as they approach the location of the Neuman boundary at $z = 0.5$ cm. The same behavior is exhibited in Fig. 24, the case where the potential is decreasing along the tunnel. The difference between the two solutions can be explained by noting that the condition enforced by the Neuman boundary in Case II (i.e., the potential is constant across $z = 0.5$ cm) is different from the condition occurring at that same location in Case I. The potential is varying at that location of the tunnel in Case I. The Neuman boundary is clearly having an effect on the solution. The imposition of a Neuman boundary

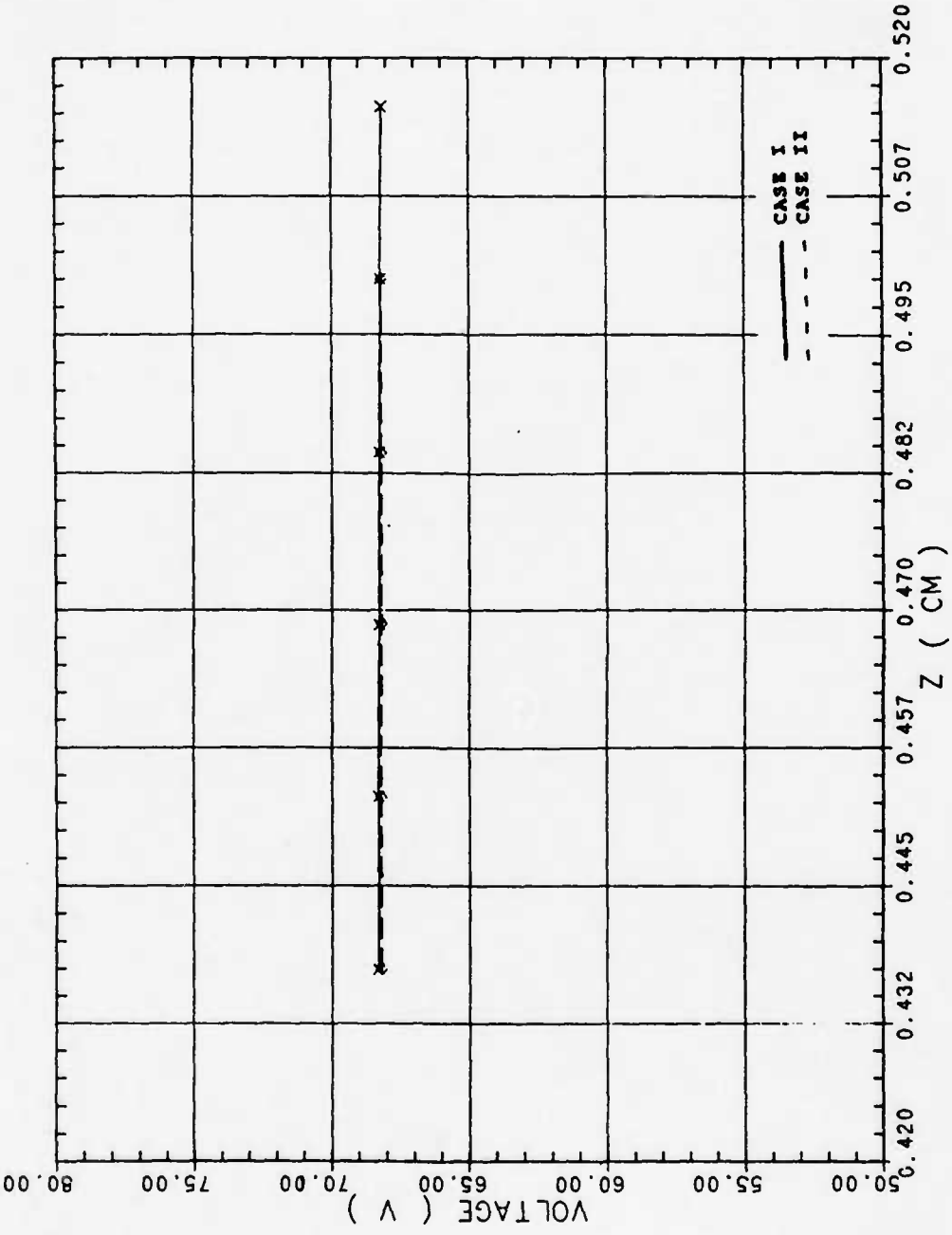

Fig. 22. Potential distribution at a fixed radius inside the tunnel of Fig. 20 (constant potential across the boundary).

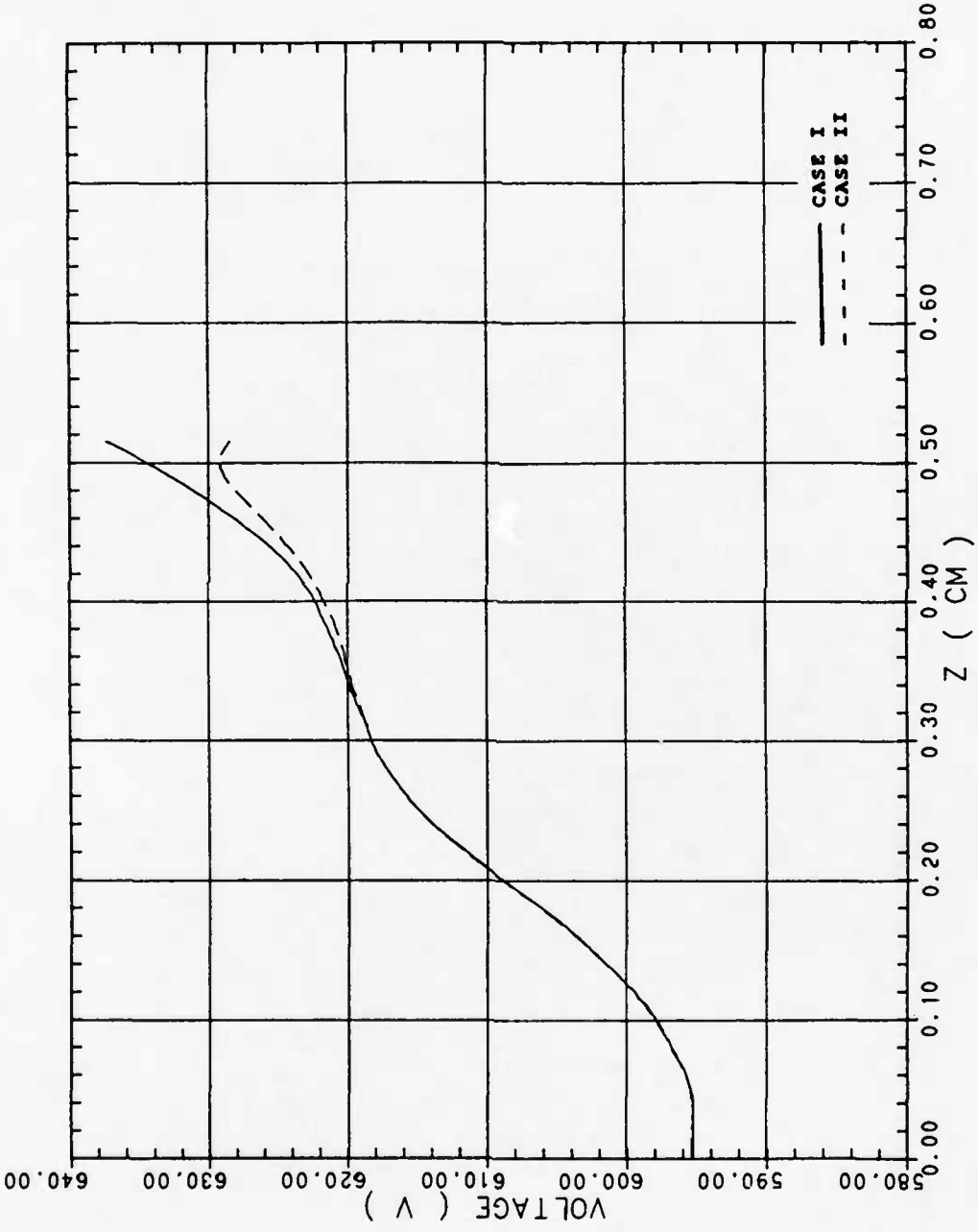

Fig. 23. Potential distribution at a fixed radius inside the tunnel of Fig. 20 (increasing potential across the boundary).

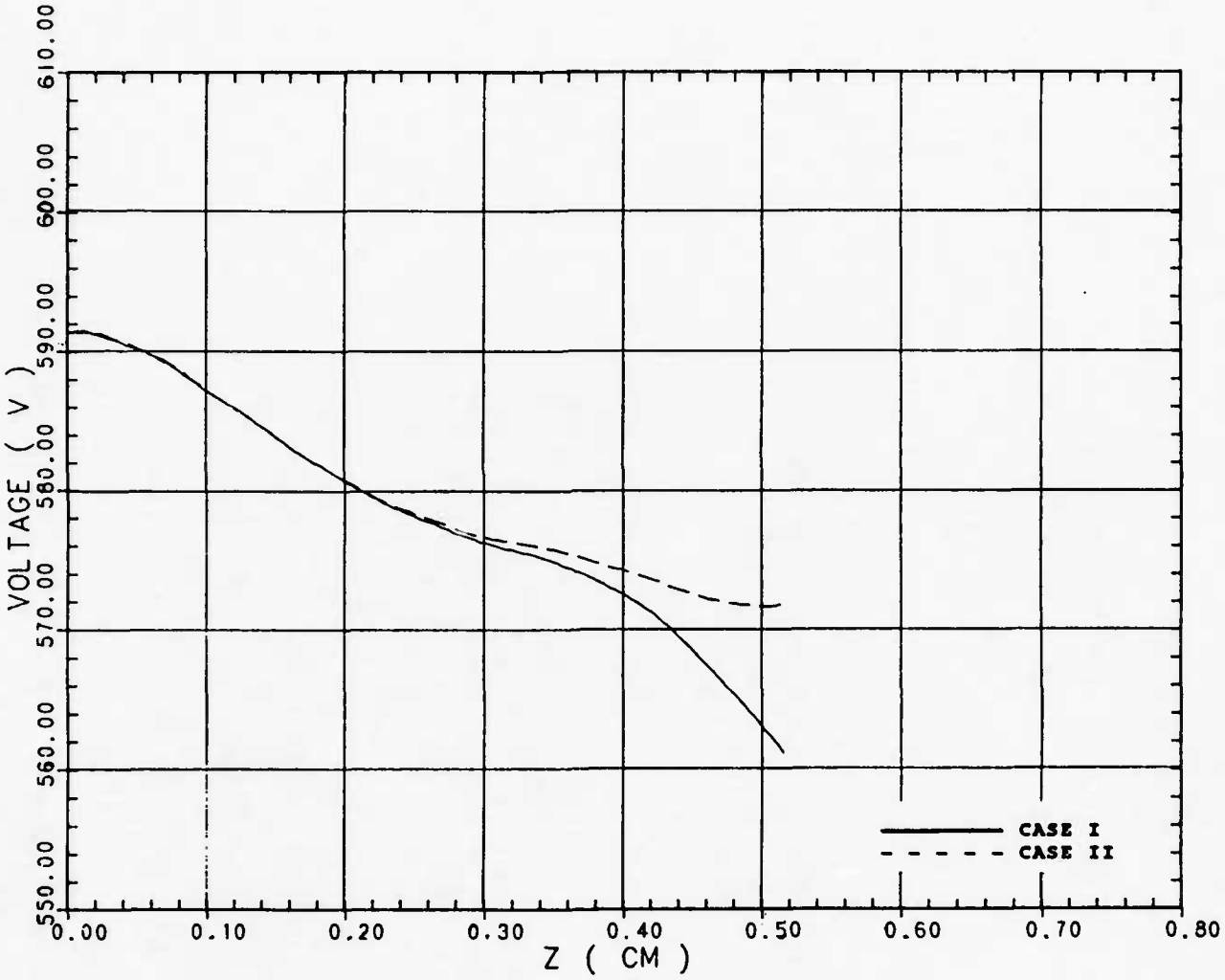

Fig. 24. Potential distribution at a fixed radius inside the tunnel of Fig. 20 (decreasing potential across the boundary).

at locations where the potential is not constant will therefore result in an erroneous solution. This is a very significant finding. This could explain the beam alteration observed in the segmentation process. Ray data injected in the continuation runs are being extracted at the Neuman boundary, and in cases where the potential is not constant across the boundary (which often is the case), these ray data are completely erroneous.

This new discovery regarding the Neuman boundary places us in a very difficult predicament. It refrains us from using the special Neuman boundary condition, which will make it virtually impossible to solve any beam optics problem. A compromise has to be found that will permit use of the special Neuman boundary and still lead to a valid solution. The plots of Figs. 23 and 24 give an indication that such a compromise is realizable. The curves, shown coincidental at some distance away from the boundary, suggest that a portion of the solution is unaffected by the error occurring at the boundary. Erroneous data could therefore be isolated by discarding the portion of the solution close to the boundary. We only have to determine how much of the solution next to the boundary is erroneous. This could be accomplished by determining the distance where the two solutions begin to deviate from each other.

To make a determination as to how far from the boundary the error propagates, a beam with a positive trajectory was again simulated with the tunnel length of 2 cm. Simulation runs similar to Case II were then made with lengths of 0.5, 1.0, and 1.5 cm. The resulting potential distributions were then compared to determine the distance the solutions of the shorter runs begin to vary from the solution of the 2 cm tunnel.

The resulting distances are presented in the plot of Fig. 25. The length of the region unaffected by the Neuman boundary (denoted by L') is shown to increase as the simulation segment length L is increased. At a simulation length of 1.5 cm, the error propagated only 0.225 cm from the Neuman boundary. This means that 85 percent of the solution is unaffected by the Neuman boundary. This very important result is the answer to our present dilemma. It suggests that the error propagating from the Neuman boundary is directly dependent on the length of the simulation. Increasing the length of simulation runs will result in an increase in the valid or usable portion of the solution and allows us to continue using the special Neuman boundary condition. (We must be reminded that the simulation lengths are still limited by the instability problem discussed earlier.)

To summarize the results obtained from this Neuman boundary study, the significant findings are enumerated as follows:

1. The use of the special Neuman boundary in beam segmentation is one cause of error in the solution process and should therefore be avoided as much as possible.
2. The solution adjacent to the Neuman boundary is erroneous and should be discarded.
3. Error propagation could be minimized by increasing the length of the simulation.

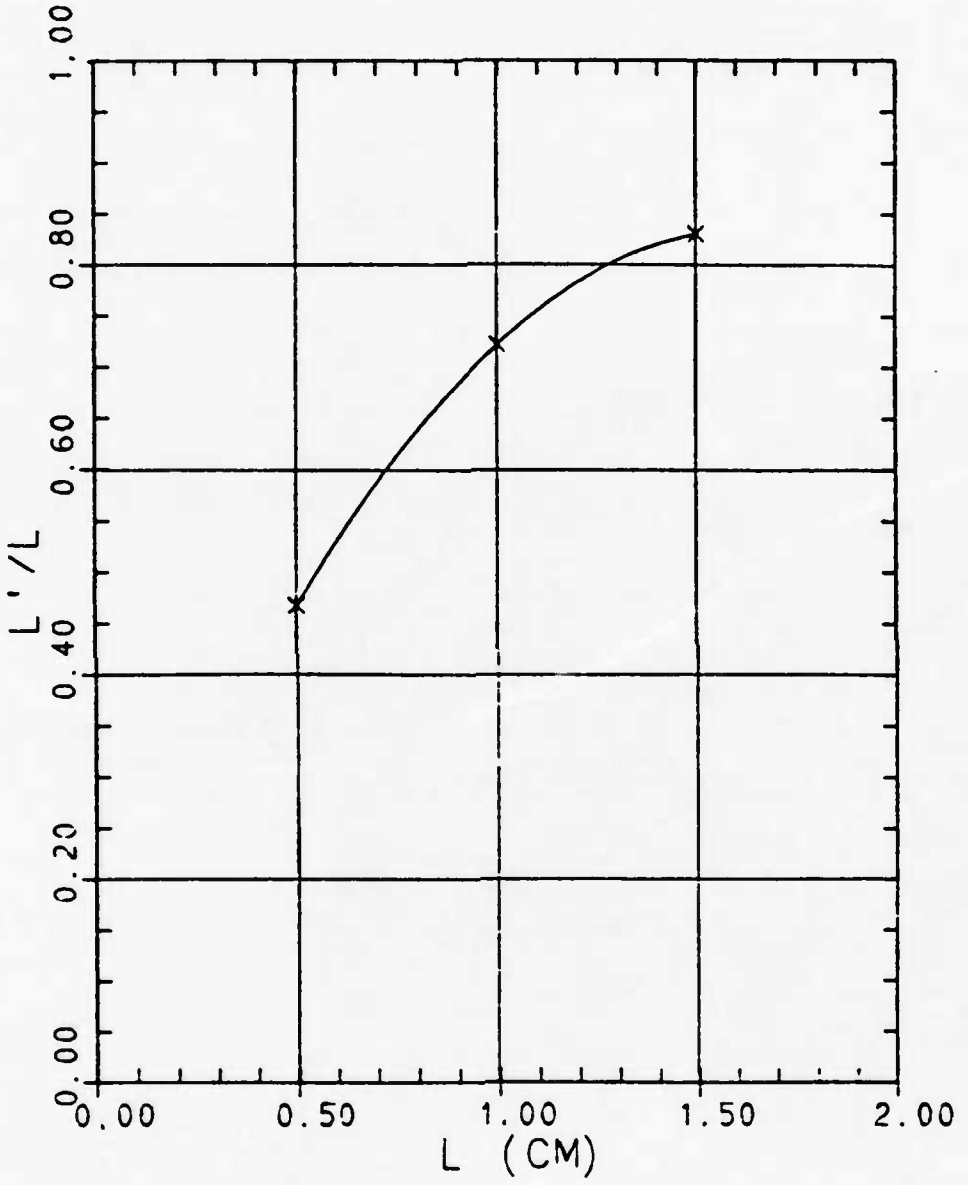

Fig. 25. Valid segment of solution as a function of simulation length.

C. Magnetic Field Effects

Another factor that was found to affect the result of the simulation was the magnetic field at the start of the simulation. Section III emphasized the importance of starting all simulations at the zero magnetic field point. Strict adherence to this restriction is very critical in the solution process. When simulation runs are ended at locations other than where B is equal to zero, the beam will have a rotation that will not be accounted for at the start of the following continuation runs. This was experienced in this study.

In all the simulation runs made in this study, actual magnetic field values were used. The magnetic field analyzer used in the measurement was set to print out the field values every 5 mils. This resulted in the location of the zero magnetic field not being discretely defined. Since the field values in the transition from +B to -B were very small (from +0.10176 G at 2.8064 cm to -0.26288 G at 2.8191 cm for the first zero crossing), the simulation was ended at the location where the field made its first sign change (at z = 2.8191 cm for the first segment). Assumption was made that the B-field value of -0.26288 G was small enough that any error occurring from it will be negligible. This assumption had a very drastic effect in the electron trajectories. This is shown in Figs. 19a and 19b. Electrons that were reaching the axis in Fig. 19b were completely diverted from their paths and caused to flow towards the tunnel wall. This resulted in a decrease in beam current in each continuation run. This contributed to the smoothing in beam trajectory and decrease in beam size demonstrated in Figs. 9 and 10.

D. R95 Values

The R95 values printed in the DEMEOS output were also found to be a potential source of error without proper interpretation. In the plots of the beam filling factor versus the axial distance, R95 values were obtained directly from the DEMEOS output. They are calculated in the code based on the beam current present at the start of the simulation. In the first simulation run, this beam current is the total current originating from the cathode minus the amount intercepted by the grid. In the continuation runs, the starting current is the total beam current from the cathode minus the current intercepted by the grid and the tunnel wall. Since R95 is defined as the radius that encloses 95 percent of the total beam current that passes through the grid, the R95 values of continuation runs are therefore erroneous. These erroneous R95 values in the continuation runs were used in the plots of Figs. 10 and 11. This error in the computation of the R95 values coupled with the increased beam interception resulting from the improper initial B-field values is another explanation for the negative emittance growth and decrease in beam size observed in the beam profile of Fig. 9.

V. MODIFICATIONS ON THE BEAM SEGMENTATION METHOD

This section deals with the modification necessary to make the solution of the present ray tracing method accurate and reliable. It introduces a new technique of data extraction and injection that greatly reduces the effect of the error emanating from the Neuman boundary. It also briefly mentions the corrections needed to account for errors due to the magnetic field and the R95 values in the continuation runs.

A. Modifications and Corrections

The following modifications to the present beam segmentation method of ray tracing are incorporated in the new ray tracing method.

1. New Ray Data Extraction Process

In view of the error propagating from the Neuman boundary, the injected ray data plane (IRD plane) was made a user-defined parameter. Previously, it was fixed to coincide with the axial location of the Neuman boundary at the end of the simulation. Now the user specifies its axial location depending on the length of the run. Subsequent simulation runs 8 cm long made to verify emittance growth showed the solution to be accurate at a distance equal to one period of the magnetic field away from the boundary. This is illustrated by the values of Table 1. The difference between the tunnel emittance values at this distance is less than 1 percent.

This change in the location of the IRD plane required a corresponding modification in the logical diagram of Fig. 2. The modified logical diagram is shown in Fig. 26. Two ray data extraction G

Table 1. Tunnel emittance and beam filling factor values obtained using the new ray tracing method.

Z(cm)	R95/A	
	(a)	(b)
2.1	0.53012	
3.1	0.61764	
4.1	0.38485	
5.1	0.68209	
6.1	0.48430	0.48494
7.1	0.49350	0.49939
8.1	0.62570	0.57645
9.1		0.58652
10.1		0.46522
11.1		0.73263
12.1		0.48014
13.1		0.56792

Z(cm)	T-Emittance	
	(a)	(b)
2.1	0.01633	
3.1	0.01240	
4.1	0.01445	
5.1	0.01750	
6.1	0.01620	0.01597
7.1	0.01620	0.01621
8.1	0.02060	0.01848
9.1		0.01714
10.1		0.01876
11.1		0.02319
12.1		0.01932
13.1		0.01992

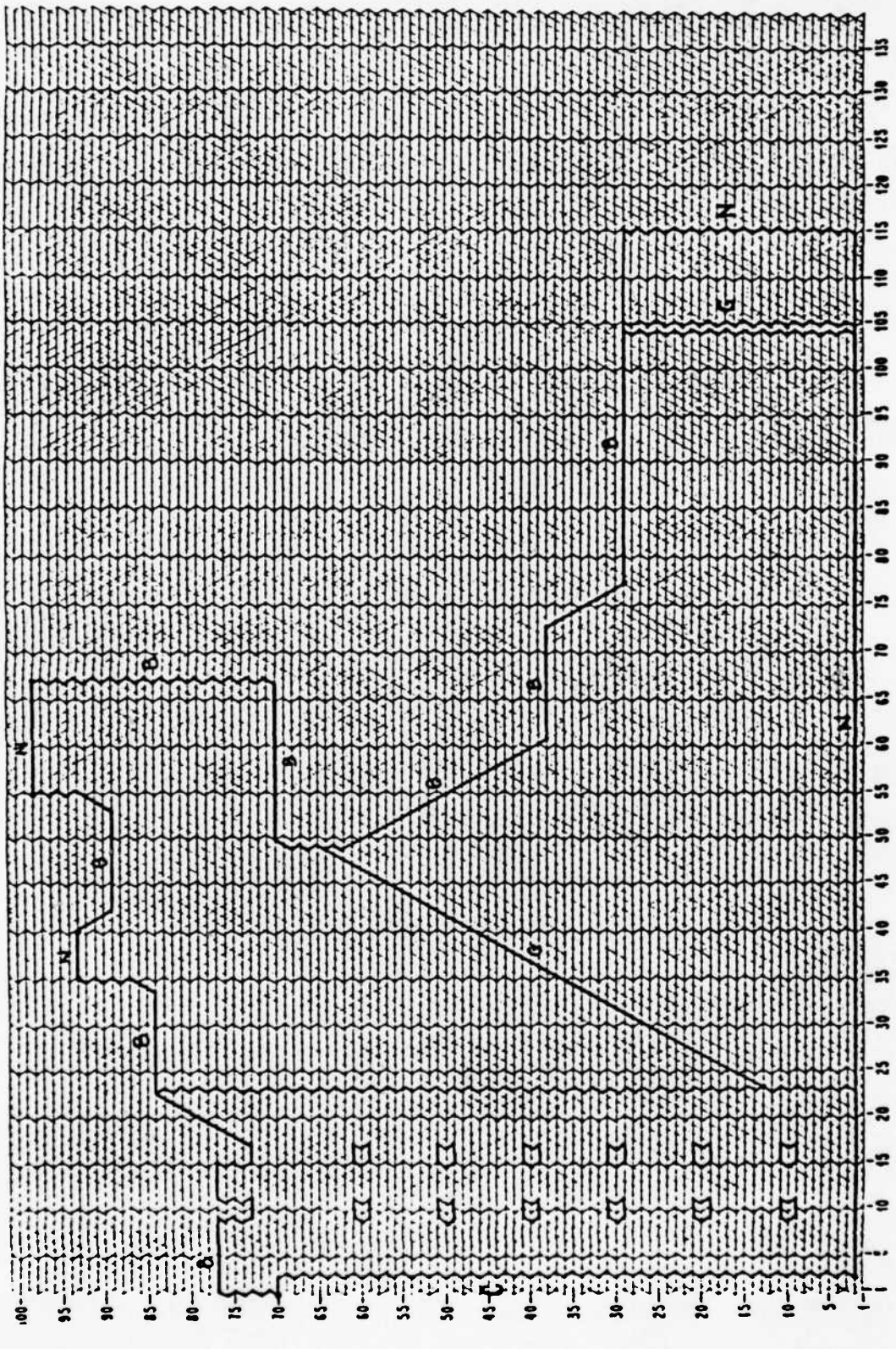

Fig. 26. Modified logical diagram for the new ray tracing method.

boundaries are placed at the axial location where ray data will be extracted. These G boundaries are configured according to Fig. 27. The potential values at the nodes of these two boundaries will be used to start the succeeding continuation runs. The first G boundary marks the position where the next simulation run will be started. The second G boundary provides the node potentials on the x-plane IRD. These potentials are crucial in the proper launching of the rays in the continuation run.

The radial and axial coordinates of each node falling on these G boundries must be exactly specified in the program, since they will be the basis for the following continuation runs. All axial nodes are separated by a distance of Δz, as shown in the figure. The radial coordinates are obtained through the code. After setting the number of nodes that will be used to describe the height of the tunnel in the logical diagram, the code is used to calculate the radial coordinates by specifying mesh generation only (CONTROL = 'M') and specifying a printout of the mesh generation result (PRINT = 'L') in a trial simulation run.

2. New Ray Data Injection Process

The Neuman boundary at the beginning of the tunnel in the continuation run was replaced by a B boundary. The logical diagram is shown in Fig. 28. Again, the two G boundaries close to the Neuman boundary at the end of the tunnel are ray data extraction boundaries. The B boundary and the combination B/G boundary at the beginning of the tunnel are ray data injection boundaries. They are configured according to Fig.

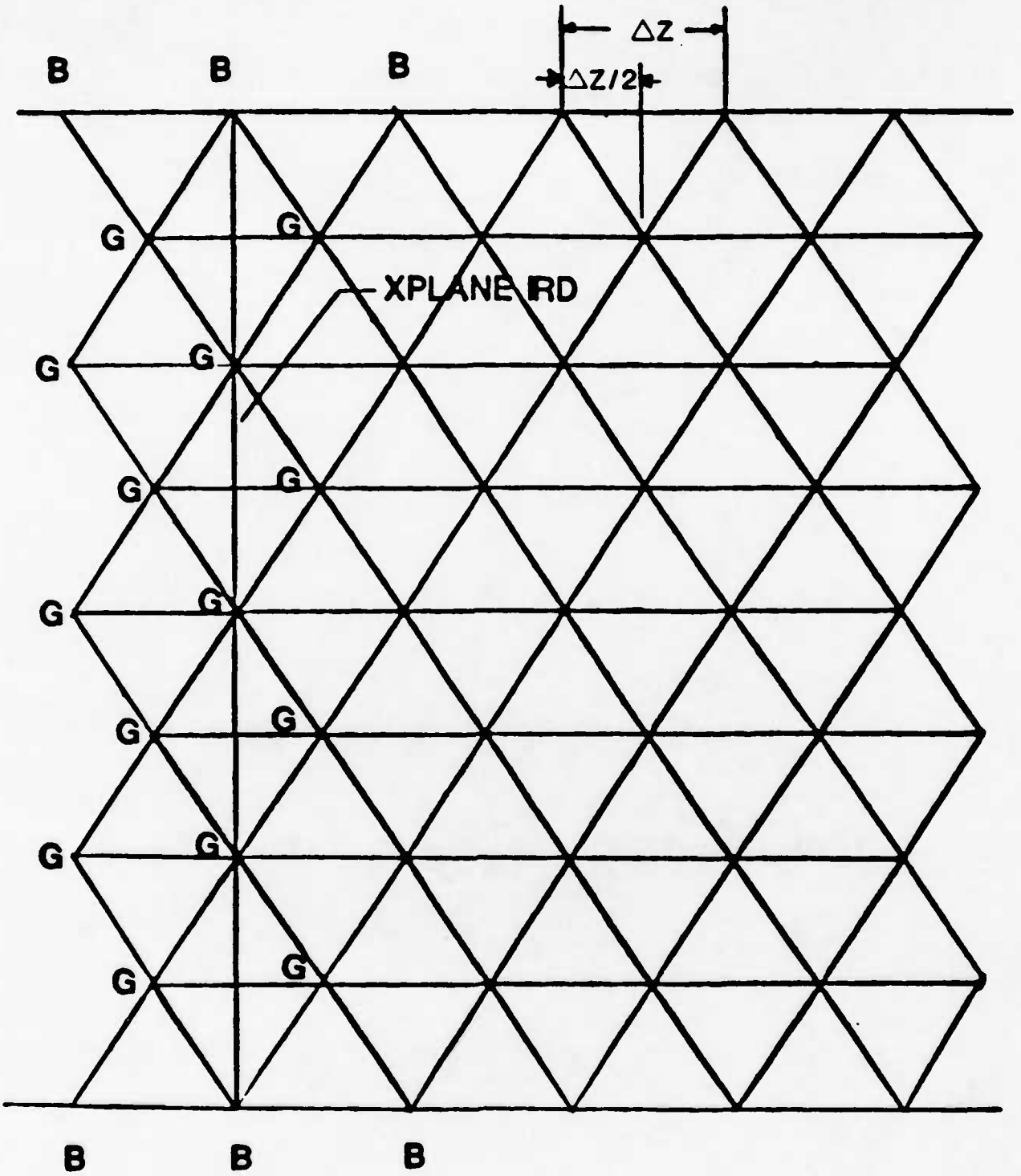

Fig. 27. Configuration of the additional G boundaries in the modified logical diagram of Fig. 26

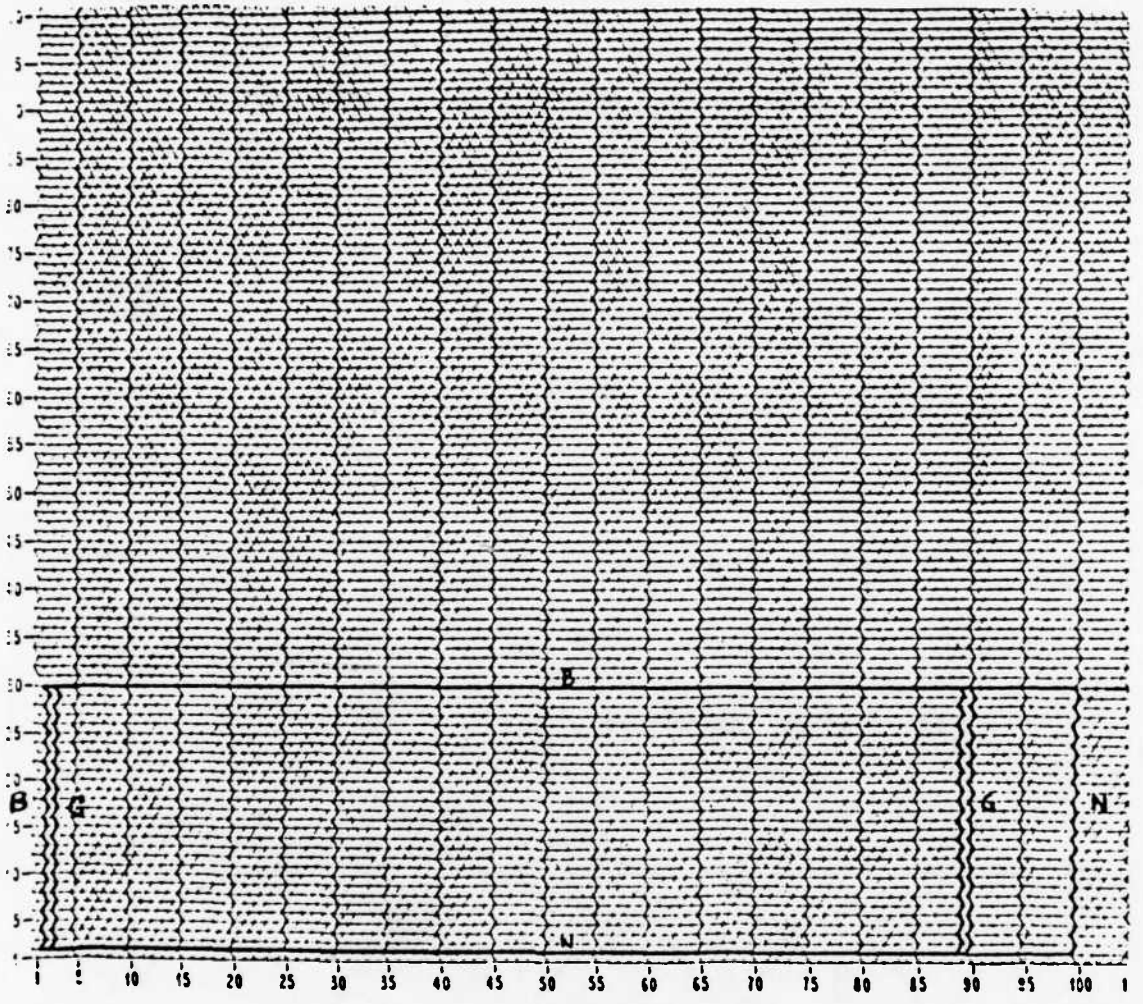

Fig. 28. Modified logical diagram for the continuation runs in the new ray tracing method

29. The potentials at the ray data extraction boundaries of the previous run are transposed here to start the simulation. The hybrid B/G boundary is used in the determination of space-charge distribution. Since the rays are not launched at the beginning of the tunnel, erroneous potentials will be set at the nodes falling on the IRD plane because of the absence of rays in the region between the B and B/G boundaries. Defining the nodes lying on the IRD plane to be B nodes fixes the potential at these nodes and bypasses the charge deposition process.

In order that the same logical diagram could be used for all continuation runs, all simulations are started at z = 0. This is not only convenient, but it also avoids any effect that a change in the logical diagram can bring in the solution. Again, the radial and axial coordinates of the nodes lying on the vertical B, B/G, and two G boundaries must be exactly specified just like in the ray data extraction process.

3. Magnetic Field Corrections

The error resulting from the magnetic field values is easily corrected by performing linear interpolation on the measured B-field. This will give us discrete zero magnetic field points that will be inserted in the B-field data set. Table 2 shows the magnetic field values, with the zero fields points incorporated.

Table 2. Magnetic field values of the B-field profile of Fig. 8.

Z (m)	B (T)	Z(m)	B (T)
0.0000000E+00	0.0000000E+00	2.1587080E-02	1.9570477E-02
1.4094000E-02	0.0000000E+00	2.1714000E-02	2.0297043E-02
1.4221000E-02	7.1231976E-06	2.1841000E-02	2.1157423E-02
1.4348000E-02	1.3737595E-05	2.1968000E-02	2.2419756E-02
1.4475000E-02	2.7475191E-05	2.2095000E-02	2.3967016E-02
1.4602000E-02	3.6124788E-05	2.2222000E-02	2.5426254E-02
1.4729000E-02	4.9862383E-05	2.2349008E-02	2.7199421E-02
1.4856000E-02	6.0547180E-05	2.2476000E-02	2.9139475E-02
1.4983000E-02	7.0723176E-05	2.2603000E-02	3.1819832E-02
1.5110000E-02	9.3110369E-05	2.2730000E-02	3.4660462E-02
1.5237000E-02	1.1040956E-04	2.2857000E-02	3.8308557E-02
1.5364000E-02	1.3279676E-04	2.2984000E-02	4.2045691E-02
1.5491000E-02	1.5518395E-04	2.3111000E-02	4.6028068E-02
1.5618000E-02	1.8774714E-04	2.3238000E-02	5.2444542E-02
1.5745000E-02	2.1725753E-04	2.3365000E-02	5.8135977E-02
1.5872000E-02	2.3455672E-04	2.3492000E-02	6.3144603E-02
1.5999000E-02	2.5847031E-04	2.3619000E-02	7.0492181E-02
1.6126000E-02	2.9815670E-04	2.3746000E-02	7.9110741E-02
1.6253000E-02	3.4140469E-04	2.3873000E-02	8.5455984E-02
1.6380000E-02	3.8465267E-04	2.4000000E-02	9.1549371E-02
1.6507000E-02	4.2281266E-04	2.4127000E-02	1.0148928E-01
1.6634000E-02	4.8285104E-04	2.4254000E-02	1.1151315E-01
1.6761000E-02	5.5560941E-04	2.4381000E-02	1.1864703E-01
1.6888000E-02	6.5177258E-04	2.4508000E-02	1.2405761E-01
1.7015000E-02	7.2605736E-04	2.4635000E-02	1.2904385E-01
1.7142000E-02	8.2985252E-04	2.4762000E-02	1.3212565E-01
1.7269000E-02	9.6417568E-04	2.4889000E-02	1.3344548E-01
1.7396000E-02	1.1264828E-03	2.5016000E-02	1.3264310E-01
1.7523000E-02	1.3106684E-03	2.5143000E-02	1.2997343E-01
1.7650000E-02	1.4902747E-03	2.5270000E-02	1.2423671E-01
1.7777000E-02	1.7060058E-03	2.5397000E-02	1.1831733E-01
1.7904000E-02	1.9319129E-03	2.5524000E-02	1.0995775E-01
1.8031000E-02	2.1903833E-03	2.5651000E-02	1.0169942E-01
1.8158000E-02	2.3989912E-03	2.5778000E-02	9.2756753E-02
1.8285000E-02	2.7063063E-03	2.5905000E-02	8.5047418E-02
1.8412000E-02	3.0853622E-03	2.6032000E-02	7.6602867E-02
1.8539000E-02	3.6221460E-03	2.6159000E-02	6.8410172E-02
1.8666000E-02	4.2220210E-03	2.6286000E-02	6.0466280E-02
1.8793000E-02	4.8722672E-03	2.6413000E-02	5.2725400E-02
1.8920000E-02	5.4741774E-03	2.6540000E-02	4.6661015E-02
1.9047000E-02	6.1351083E-03	2.6667000E-02	4.1347109E-02
1.9174000E-02	7.1303208E-03	2.6794000E-02	3.6290148E-02
1.9301000E-02	7.9891749E-03	2.6921000E-02	3.1360895E-02
1.9428000E-02	8.8704162E-03	2.7048000E-02	2.6950618E-02
1.9555000E-02	9.6346336E-03	2.7175000E-02	2.3308120E-02
1.9682000E-02	1.0336269E-02	2.7302000E-02	1.9679360E-02
1.9809000E-02	1.1047062E-02	2.7429000E-02	1.6555838E-02
1.9936000E-02	1.1762943E-02	2.7556000E-02	1.1743609E-02
2.0063000E-02	1.2538863E-02	2.7683000E-02	8.4699907E-03
2.0190000E-02	1.3181986E-02	2.7810000E-02	5.8227052E-03
2.0317000E-02	1.3865304E-02	2.7937000E-02	2.9820758E-03
2.0444000E-02	1.4427528E-02	2.8064000E-02	1.0175997E-05
2.0571000E-02	1.5150024E-02	2.8099400E-02	0.0000000E+00
2.0698000E-02	1.5652209E-02	2.8191000E-02	-2.6287991E-05
2.0825000E-02	1.6269383E-02	2.8318000E-02	-4.6453424E-03
2.0952000E-02	1.6690161E-02	2.8445000E-02	-9.6900927E-03
2.1079000E-02	1.7197434E-02	2.8572000E-02	-1.4461787E-02
2.1206000E-02	1.7702672E-02	2.8699000E-02	-2.0078937E-02
2.1333000E-02	1.8275581E-02	2.8826000E-02	-2.6095495E-02
2.1460000E-02	1.8806768E-02	2.8953000E-02	-3.1637173E-02

Table 2. Continued.

Z (m)	B (T)	Z (m)	B (T)
2.9080000E-02	-3.8464419E-02	3.6700000E-02	-1.3528648E-01
2.9207000E-02	-4.6001441E-02	3.6827000E-02	-1.4897235E-01
2.9334000E-02	-5.4191422E-02	3.6954000E-02	-1.6269553E-01
2.9461000E-02	-6.2935995E-02	3.7081000E-02	-1.7472780E-01
2.9588000E-02	-7.3250215E-02	3.7208000E-02	-1.8888006E-01
2.9715000E-02	-8.4144468E-02	3.7335000E-02	-2.0186972E-01
2.9842000E-02	-9.5507664E-02	3.7462000E-02	-2.1224161E-01
2.9969000E-02	-1.0891454E-01	3.7589000E-02	-2.2105741E-01
3.0096000E-02	-1.2375369E-01	3.7716000E-02	-2.2858341E-01
3.0223000E-02	-1.3946034E-01	3.7843000E-02	-2.3365699E-01
3.0350000E-02	-1.5501180E-01	3.7970000E-02	-2.3672421E-01
3.0477000E-02	-1.7035890E-01	3.8097000E-02	-2.3751200E-01
3.0604000E-02	-1.8409904E-01	3.8224000E-02	-2.3604581E-01
3.0731000E-02	-1.9765601E-01	3.8351000E-02	-2.3286920E-01
3.0858000E-02	-2.0867407E-01	3.8478000E-02	-2.2673223E-01
3.0985000E-02	-2.1831244E-01	3.8605000E-02	-2.1831244E-01
3.1112000E-02	-2.2673223E-01	3.8732000E-02	-2.0867407E-01
3.1239000E-02	-2.3286920E-01	3.8859000E-02	-1.9765601E-01
3.1366000E-02	-2.3604581E-01	3.8986000E-02	-1.8409904E-01
3.1493000E-02	-2.3751200E-01	3.9113000E-02	-1.7035890E-01
3.1620000E-02	-2.3672421E-01	3.9240000E-02	-1.5501180E-01
3.1747000E-02	-2.3365699E-01	3.9367000E-02	-1.3946034E-01
3.1874000E-02	-2.2858341E-01	3.9494000E-02	-1.2375369E-01
3.2001000E-02	-2.2105741E-01	3.9621000E-02	-1.0891454E-01
3.2128000E-02	-2.1224161E-01	3.9748000E-02	-9.5507664E-02
3.2255000E-02	-2.0186972E-01	3.9875000E-02	-8.4144468E-02
3.2382000E-02	-1.8888006E-01	4.0002000E-02	-7.3250215E-02
3.2509000E-02	-1.7472780E-01	4.0129000E-02	-6.2935995E-02
3.2636000E-02	-1.6269553E-01	4.0256000E-02	-5.4191422E-02
3.2763000E-02	-1.4897235E-01	4.0383000E-02	-4.6001441E-02
3.2890000E-02	-1.3528648E-01	4.0510000E-02	-3.8464419E-02
3.3017000E-02	-1.2150225E-01	4.0637000E-02	-3.1637173E-02
3.3144000E-02	-1.0912145E-01	4.0764000E-02	-2.6095495E-02
3.3271000E-02	-9.5634016E-02	4.0891000E-02	-2.0078937E-02
3.3398000E-02	-8.4492148E-02	4.1018000E-02	-1.4461787E-02
3.3525000E-02	-7.4612103E-02	4.1145000E-02	-9.6900927E-03
3.3652000E-02	-6.6175354E-02	4.1272000E-02	-4.6453424E-03
3.3779000E-02	-5.8121052E-02	4.1399000E-02	-2.6287991E-05
3.3906000E-02	-5.0555199E-02	4.1462500E-02	0.0000000E+00
3.4033000E-02	-4.4989777E-02	4.1526000E-02	2.6287991E-05
3.4160000E-02	-4.0195186E-02	4.1653000E-02	4.6453424E-03
3.4287000E-02	-3.7102532E-02	4.1780000E-02	9.6900927E-03
3.4414000E-02	-3.4405892E-02	4.1907000E-02	1.4461787E-02
3.4541000E-02	-3.2097637E-02	4.2034000E-02	2.0078937E-02
3.4668000E-02	-3.0717942E-02	4.2161000E-02	2.6095495E-02
3.4795000E-02	-2.9901318E-02	4.2288000E-02	3.1637173E-02
3.4922000E-02	-3.0717942E-02	4.2415000E-02	3.8464419E-02
3.5049000E-02	-3.2097637E-02	4.2542000E-02	4.6001441E-02
3.5176000E-02	-3.4405892E-02	4.2669000E-02	5.4191422E-02
3.5303000E-02	-3.7102532E-02	4.2796000E-02	6.2935995E-02
3.5430000E-02	-4.0195186E-02	4.2923000E-02	7.3250215E-02
3.5557000E-02	-4.4989777E-02	4.3050000E-02	8.4144468E-02
3.5684000E-02	-5.0555199E-02	4.3177000E-02	9.5507664E-02
3.5811000E-02	-5.8121052E-02	4.3304000E-02	1.0891454E-01
3.5938000E-02	-6.6175354E-02	4.3431000E-02	1.2375369E-01
3.6065000E-02	-7.4612103E-02	4.3558000E-02	1.3946034E-01
3.6192000E-02	-8.4492148E-02	4.3685000E-02	1.5501180E-01
3.6319000E-02	-9.5634016E-02	4.3812000E-02	1.7035890E-01
3.6446000E-02	-1.0912145E-01	4.3939000E-02	1.8409904E-01
3.6573000E-02	-1.2150225E-01	4.4066000E-02	1.9765601E-01

Table 2. Continued.

Z(m)	B (T)	Z (m)	B(T)
4.4193000E-02	2.0867407E-01	5.1813000E-02	2.2673223E-01
4.4320000E-02	2.1831244E-01	5.1940000E-02	2.1831244E-01
4.4447000E-02	2.2673223E-01	5.2067000E-02	2.0867407E-01
4.4574000E-02	2.3286920E-01	5.2194000E-02	1.9765601E-01
4.4701000E-02	2.3604581E-01	5.2321000E-02	1.8409904E-01
4.4828000E-02	2.3751200E-01	5.2448000E-02	1.7035890E-01
4.4955000E-02	2.3672421E-01	5.2575000E-02	1.5501180E-01
4.5082000E-02	2.3365699E-01	5.2702000E-02	1.3946034E-01
4.5209000E-02	2.2858341E-01	5.2829000E-02	1.2375369E-01
4.5336000E-02	2.2105741E-01	5.2956000E-02	1.0891454E-01
4.5463000E-02	2.1224161E-01	5.3083000E-02	9.5507664E-02
4.5590000E-02	2.0186972E-01	5.3210000E-02	8.4144468E-02
4.5717000E-02	1.8888006E-01	5.3337000E-02	7.3250215E-02
4.5844000E-02	1.7472780E-01	5.3464000E-02	6.2935995E-02
4.5971000E-02	1.6269553E-01	5.3591000E-02	5.4191422E-02
4.6098000E-02	1.4897235E-01	5.3718000E-02	4.6001441E-02
4.6225000E-02	1.3528648E-01	5.3845000E-02	3.8464419E-02
4.6352000E-02	1.2150225E-01	5.3972000E-02	3.1637173E-02
4.6479000E-02	1.0912145E-01	5.4099000E-02	2.6095495E-02
4.6606000E-02	9.5634016E-02	5.4226000E-02	2.0070937E-02
4.6733000E-02	8.4492148E-02	5.4353000E-02	1.4461787E-02
4.6860000E-02	7.4612103E-02	5.4480000E-02	9.6900927E-03
4.6987000E-02	6.6175354E-02	5.4607000E-02	4.6453424E-03
4.7114000E-02	5.8121052E-02	5.4734000E-02	2.6287991E-05
4.7241000E-02	5.0555199E-02	5.4797500E-02	0.0000000E+00
4.7368000E-02	4.4989777E-02	5.4861000E-02	-2.6287991E-05
4.7495000E-02	4.0195186E-02	5.4988000E-02	-4.6453424E-03
4.7622000E-02	3.7102532E-02		
4.7749000E-02	3.4405892E-02		
4.7876000E-02	3.2097637E-02		
4.8003000E-02	3.0717942E-02		
4.8130000E-02	2.9901318E-02		
4.8257000E-02	3.0717942E-02		
4.8384000E-02	3.2097637E-02		
4.8511000E-02	3.4405892E-02		
4.8638000E-02	3.7102532E-02		
4.8765000E-02	4.0195186E-02		
4.8892000E-02	4.4989777E-02		
4.9019000E-02	5.0555199E-02		
4.9146000E-02	5.8121052E-02		
4.9273000E-02	6.6175354E-02		
4.9400000E-02	7.4612103E-02		
4.9527000E-02	8.4492148E-02		
4.9654000E-02	9.5634016E-02		
4.9781000E-02	1.0912145E-01		
4.9908000E-02	1.2150225E-01		
5.0035000E-02	1.3528648E-01		
5.0162000E-02	1.4897235E-01		
5.0289000E-02	1.6269553E-01		
5.0416000E-02	1.7472780E-01		
5.0543000E-02	1.8888006E-01		
5.0670000E-02	2.0186972E-01		
5.0797000E-02	2.1224161E-01		
5.0924000E-02	2.2105741E-01		
5.1051000E-02	2.2858341E-01		
5.1178000E-02	2.3365699E-01		
5.1305000E-02	2.3672421E-01		
5.1432000E-02	2.3751200E-01		
5.1559000E-02	2.3604581E-01		
5.1686000E-02	2.3286920E-01		

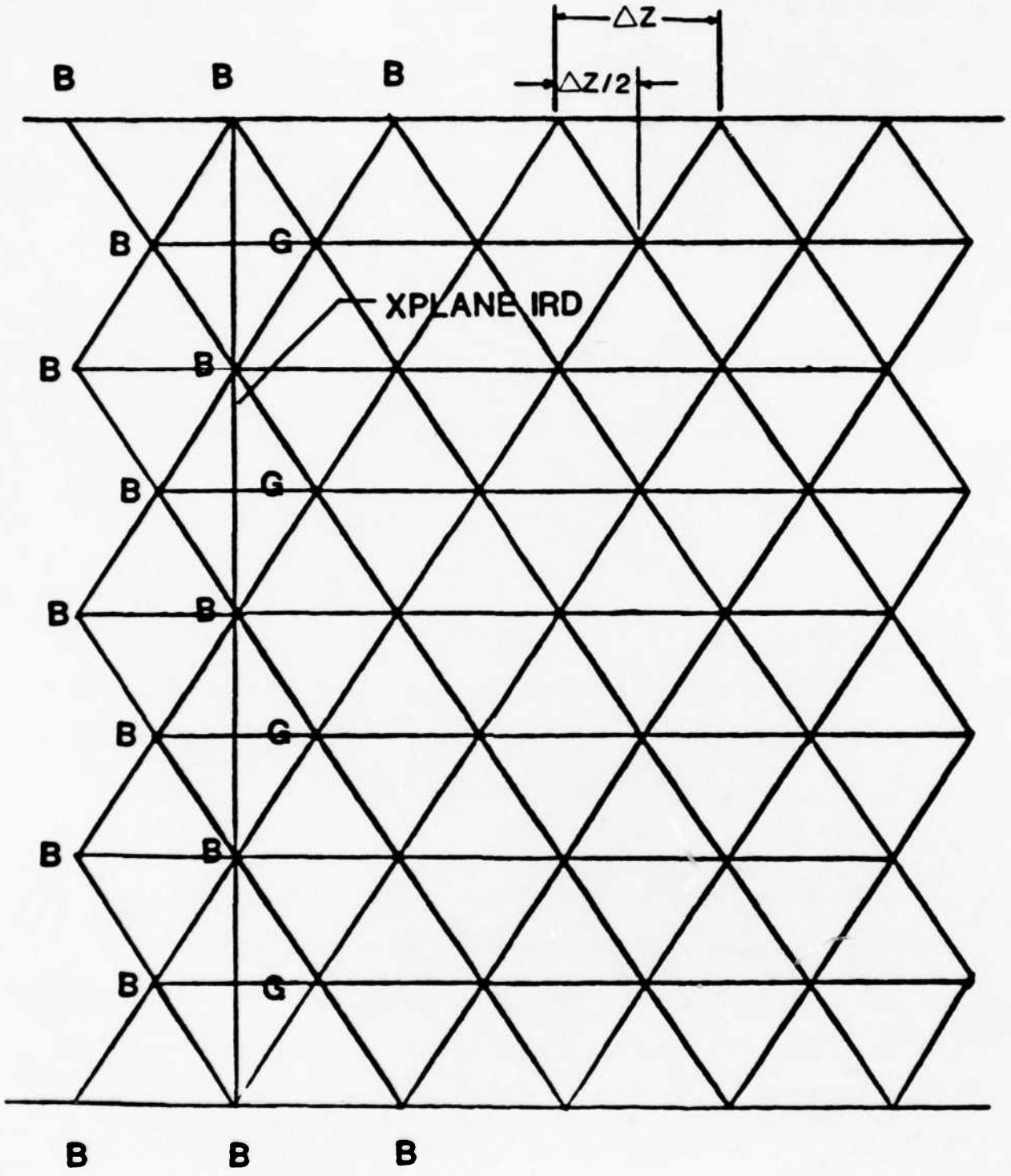

Fig. 29. Configuration of the B and B/G boundaries in the modified logical diaagram of Fig. 28.

4. R95 Value Corrections

The error caused by the erroneous R95 values is avoided by recalculating the R95 values in the continuation runs. The correct values are obtained by using the beam current present in the initial simulation in all computations.

B. Simulation Using the New Method

These modifications and corrections brought about a stair-step method of beam segmentation. In this new approach, the segments included in each simulation run are made to overlap each other. Figure 30 illustrates this overlapping process. Simulation 'a' covers the segment from the cathode up to a distance of approximately 8 cm downstream. Simulation 'b' (starting and ending at $z = 5.5$ cm and $z = 13.6$ cm, respectively) overlaps and resolves the end section of simulation 'a', allowing us to discard the solution adjacent to the Neuman boundary.

Simulation performed in Section III was repeated using this new beam segmentation method. The resulting beam profile is shown in Fig. 31a. It is remarkably in good agreement with the beam profile of Fig. 12. The plots of the beam filling factor and tunnel emittance for the beam profile of Figs. 12 and 35 (shown in Figs. 32 and 33) clearly illustrate this agreement between the two solutions. To further illustrate the improved accuracy resulting from this new method of beam segmentation, the curves of Figs. 32 and 33 are plotted along with the beam filling factor and tunnel emittance obtained using the old beam segmentation method. These curves are shown in Figs. 34 and 35.

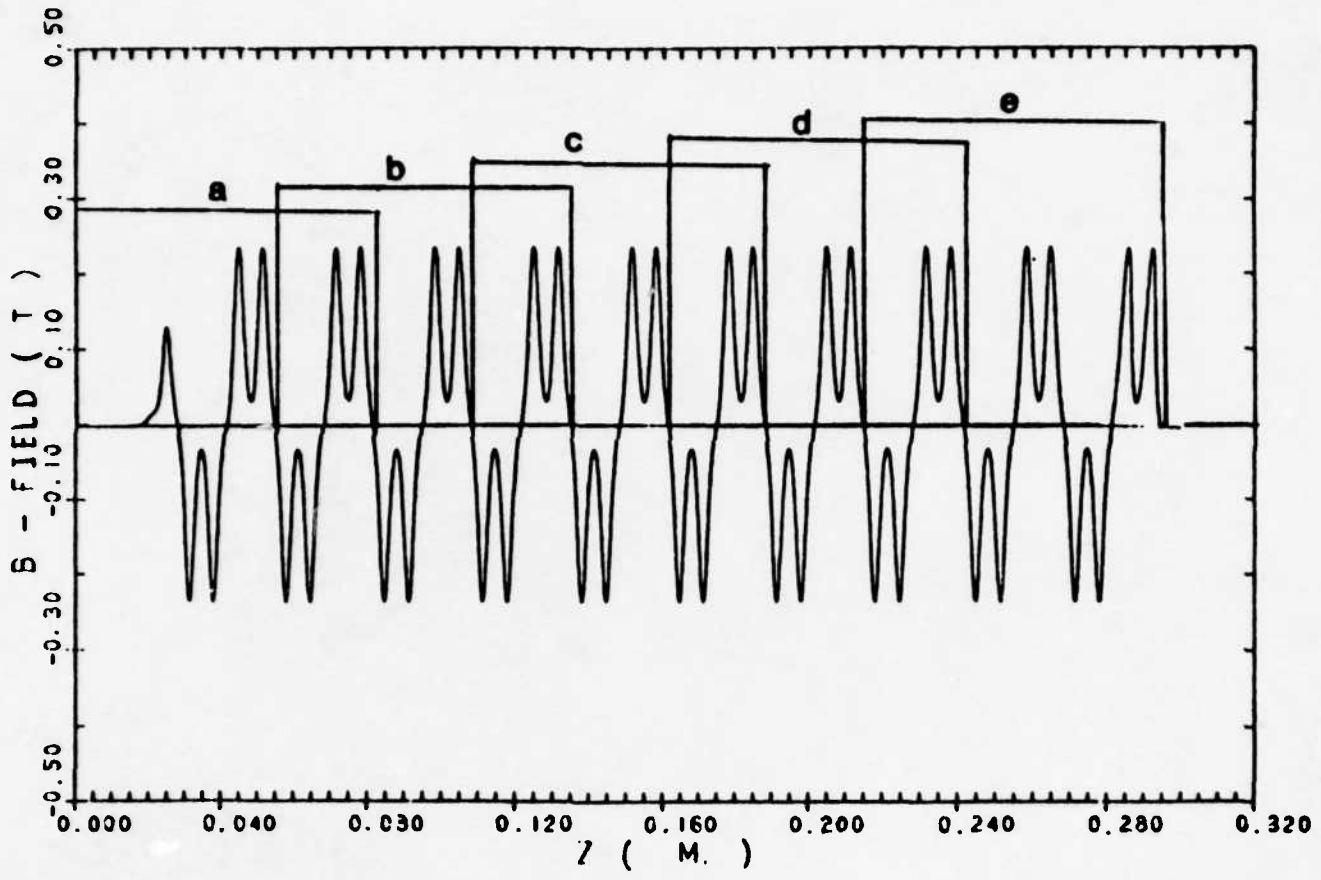

Fig. 30. Periods of magnetic fields included in each simulation run using the new ray tracing method.

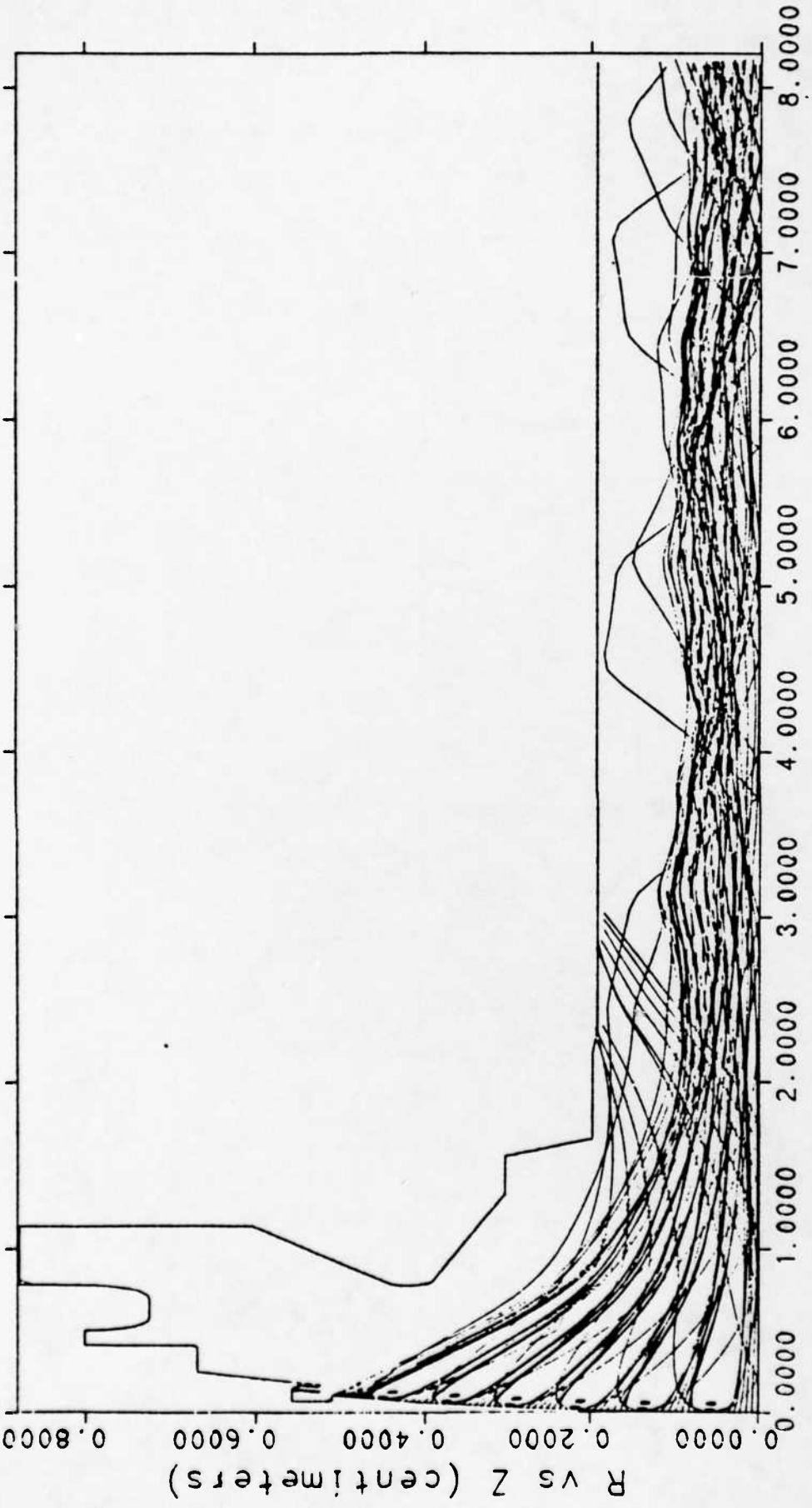

Fig. 31. Electron trajectories using the new method to verify tunnel emittance growth.

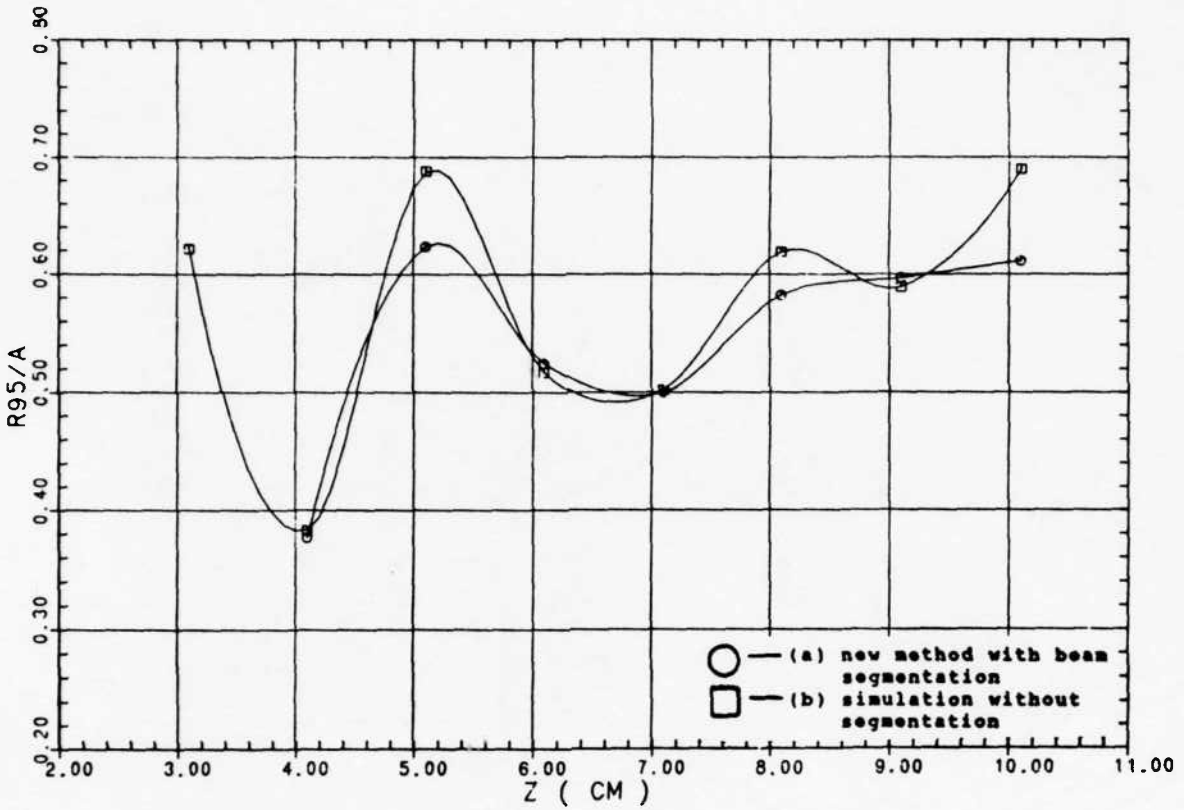

Fig. 32. Beam filling factor versus axial distance using (a) the new method with beam segmentation, and (b) simulation without segmentation.

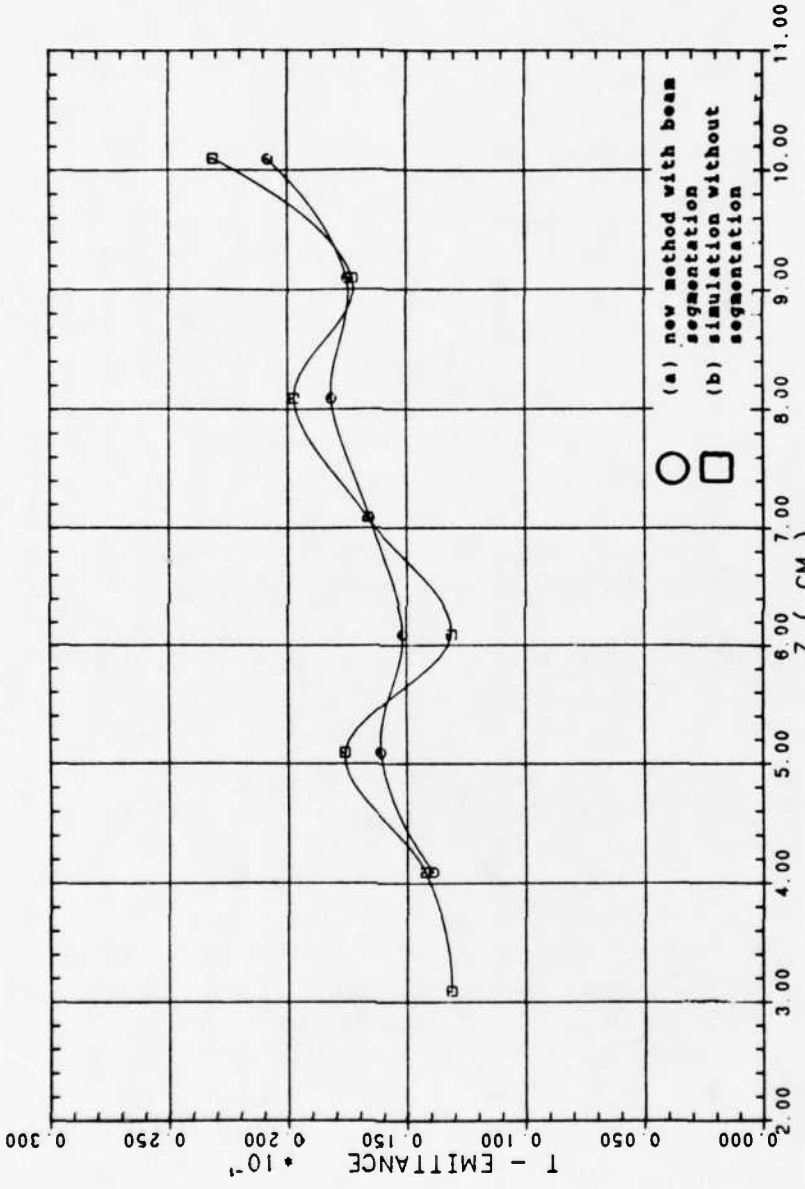

Fig. 33. Tunnel emittance versus axial distance using (a) the new method with beam segmentation, and (b) simulation without segmentation.

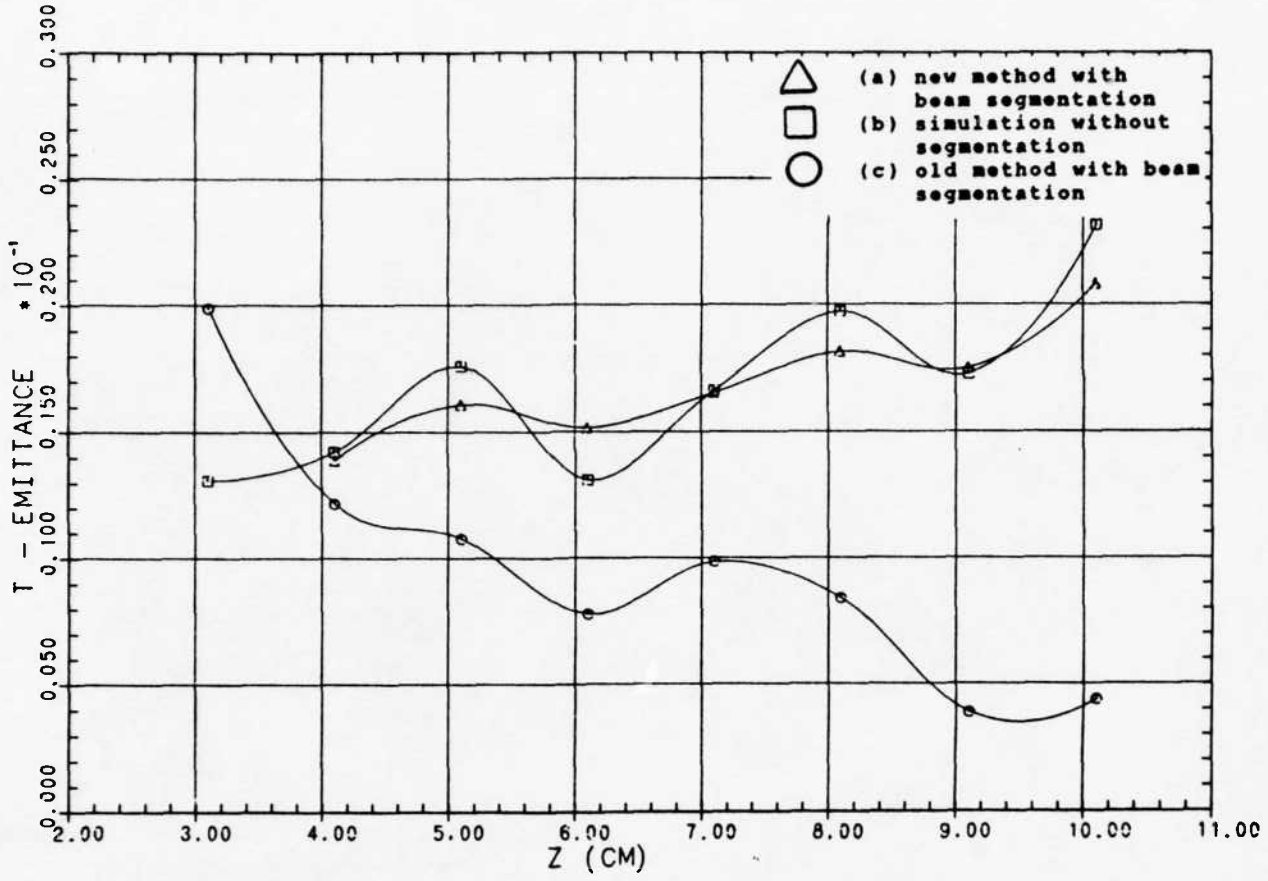

Fig. 34. Tunnel emittance versus axial distance using (a) the new method with beam segmentation, (b) simulation without segmentation, and (c) the old method with beam segmentation.

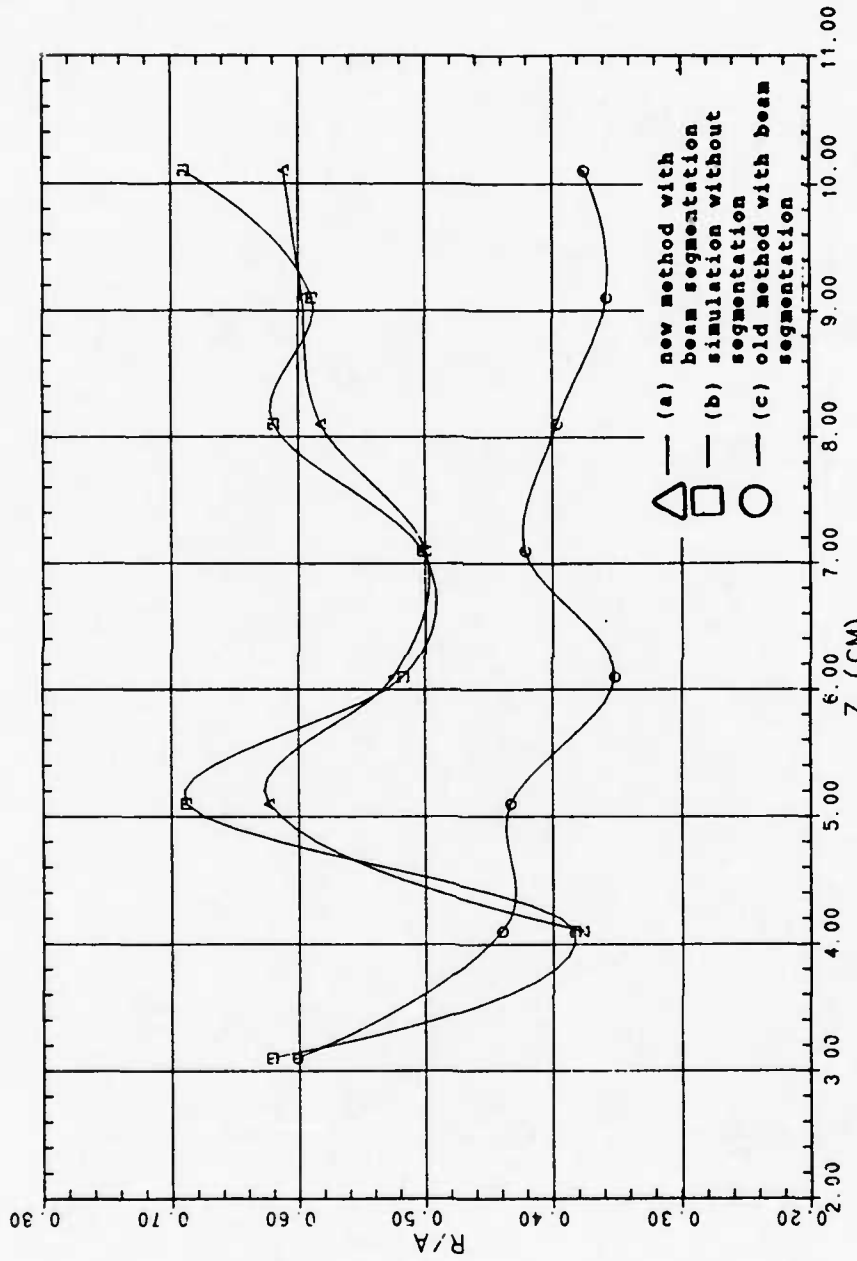

Fig. 35. Beam filling factor versus axial distance using (a) the new method with beam segmentation, (b) simulation without segmentation, and (c) the old method with beam segmentation.

VI. THE NEW RAY TRACING METHOD

This section is a formal presentation of the ray tracing method that incorporates the modifications discussed in the previous section. The step-by-step procedure is demonstrated through an example. Brief discussions are included to clarify and bring up important details that will allow DEMEOS users to perform ray tracing without any difficulty.

A. Ray Tracing Procedure

The previous section presented a simulation using this new method of beam segmentation. That simulation will be referred to as each step of the ray tracing procedure is presented. Figures enclosed in parentheses are actual values used in the simulations.

The ray tracing procedure is divided into two steps:

1. Modeling and simulation of the gun and its magnetics.
2. Extraction and injection of ray data in the continuation runs.

Since the difference between the new and the old method of ray tracing lies mainly in the continuation process, only the process of extracting and injecting of ray data will be presented. Modifications that will affect the simulations in the gun region will be pointed out as they come up.

1. Ray Data Extraction

1. Adjust the simulation length to include at least four periods of the magnetic field. In the example, the first single-peak and four periods of the double-peak magnetic fields were included in the first simulation run. This is shown as segment 'a' in Fig. 30.

2. Define x-plane IRD to be the axial coordinate of the next to last zero B-field location. (This is at z = 5.47975 cm in the example.) Note that at least one extra field point after the last zero B field is needed to properly run DEMEOS. Also, all zero B-field locations must be discretely defined in the magnetic field data set.
3. Modify the logical diagram of the gun region by adding two G boundaries in the tunnel region, as shown in Fig. 26. The G boundary closest to the Neuman boundary at the end of the region should coincide with the location of the x-plane IRD (the plane where injected ray data will be extracted). The other G boundary is positioned at a distance of Δz away from the x-plane IRD, as shown in Fig. 27. This distance is calculated as follows:

$$\Delta z = L/N$$

where

L = length of simulation run

N = node number defining the axial end of the run

Note that the recessed nodes (odd numbered J's) are positioned at a distance of $\Delta z/2$ from x-plane IRD.

In the example, node No. 215 was set for the end of the first region at z = 8.14675 cm. Dividing this value of z by 215 gives a Δz of 0.03789 cm. Dividing the axial distance of the x-plane IRD (z = 5.47975 cm) by Δz gives 144.62. Rounding off gives node No. 145 for both the x-plane IRD and the second G boundary. With this value of Δz, the second G boundary has axial coordinates of 5.47975

cm for even numbered J's and 5.49870 cm for odd numbered ones. Similarly, the first G boundary (at node No. 144) has axial coordinates 5.44186 cm and 5.46080 cm, respectively.

4. Tighten the tolerance to increase the accuracy of the solution. The following convergence tolerances were used in the example:

ALPHA-1 = 1.500	ALPHA-2 = L.50	ALPHA-2 = 1.300
EPS-1 = 0.003	EPS-2 = 0.01	EPS-V = 0.003

Note that convergence to within these specified tolerances may not be completely met. In simulation runs made for this study, it was observed that data away from the end of the run will reach stability even if the tolerances are not completely satisfied. Simulation could be terminated once the solution past the x-plane IRD becomes stable and solutions up to the x-plane IRD can be considered to have converged. It will be helpful to define at least two x-planes after the x-plane IRD so that comparison of the solutions in the overlapping segments could be made. Figure 30 illustrates how the simulation runs overlap. The end segments of each run are included in succeeding simulation runs.

2. Ray Data Injection

1. Adjust the simulation length to include at least four periods of the magnetic field. In the example, six periods of the double-peak periods are included in the first continuation run, resulting in a simulation length of 8 cm. This is shown in Fig. 30 as segment 'b'.

2. Outline the tunnel according to the logical diagram of Fig. 28. The two G boundaries near the Neuman boundary follow the discussion in the data extraction process.
3. Start the simulation at z = 0. This means that the vertical B boundary will have an axial coordinate of a = 0 cm for even numbered J's, and $\Delta z/2$ (0.03789 cm/2) for the odd numbered J's.
4. Configure the B/G boundary according to Fig. 29. The B and G nodes have axial coordinates equal to Δz (0.03789 cm) and 1.5 Δz (0.05684 cm), respectively.
5. Subtract the beam voltage potential (26,000 V) from the potentials at each of the nodes on the two G boundaries discussed in the data extraction process. Transpose the resulting values to the nodes of the B and B/G boundary. The first G boundary corresponds to the vertical B boundary, while the second G boundary corresponds to the combination B/G boundary.
6. Since the rays are not launched at the start of the simulation, the restriction that the magnetic field be zero at the start of the simulation does not apply. However, the field must be zero at the location where the rays are launched (at z = 0.03789 cm). At least two extra field points (one before the start of the region, and another after the end) are needed to properly run DEMEOS.
7. Tighten the tolerance to increase the accuracy of the solution. Set the convergence tolerances according to the values given in step 4 of the ray data extraction process.
8. Reset the x values of the rays in the injected ray data file to zero.

Since we are simulating segments of considerable length, it will take several iterations before the solution reaches convergence. Again, we do not have to attain complete convergence of the entire solution. As soon as the solution past the x-plane IRD becomes stable, convergence of the solution can be assumed. This is one aspect of this beam segmentation process that is very advantageous. We are not interested in the solution past the IRD plane, since they are going to be discarded anyway. Again, it is recommended that at least two x-planes after the x-plane IRD be defined to help us in determining the stability of the solution.

To reach a convergence in the potential of 0.003 percent ($\Delta v_{i,j}/v_{i,j} < 0.00003$) sometimes requires an abnormal amount of computer time. To avoid excessive run times, it is recommended that LOOPMAX be set equal to a value less than or equal to 10 and set SAV = 'B'. This saves the output of the simulation after the 10th iteration, allowing evaluation of intermediate solution. To start the 11th loop/iteration, set SAVD = 'Y'. This instructs the code to use the result of the last iteration as initial condition. Remember that an output and input file must be defined in these processes.

All continuation runs are set up in similar fashion. No changes in the logical diagram is needed as long as the segments included in each simulation are kept the same.

VII. CONCLUSIONS

As mentioned in the beginning of this report, the need to verify emittance growth is the motivation behind this study. Because of the inconsistencies discovered in the present ray tracing method, highly accurate simulation over the full length of the tube was not possible. This thwarted our investigation of beam behavior and compelled us to deviate from our initial objective. We proceeded to investigate the causes of the inconsistencies in the ray tracing approach and developed a method that could be used in verifying a very sensitive parameter, such as tunnel emittance. Now that we are able to accurately trace the beam over the full length of the tube, we could proceed to verify occurrence of emittance growth.

A. Verification of Emittance Growth

Simulation of the entire length of the tube was made by continuing the simulations performed in Section V.B. The beam was traced up to a distance of approximately 30 cm downstream. The beam profile resulting from this simulation is shown in Figs. 36a, b, c, d, and e. The length of the segments and the periods of magnetic field included in each simulation run are depicted in Fig. 30. Figures 37 and 38 show the plots of the beam size and tunnel emittance for this beam. Tables 3 and 4 show the values used in these two figures. It also demonstrates that the distance of 1 period of magnetic field away from the Neuman boundary is sufficient to obtain error free solutions.

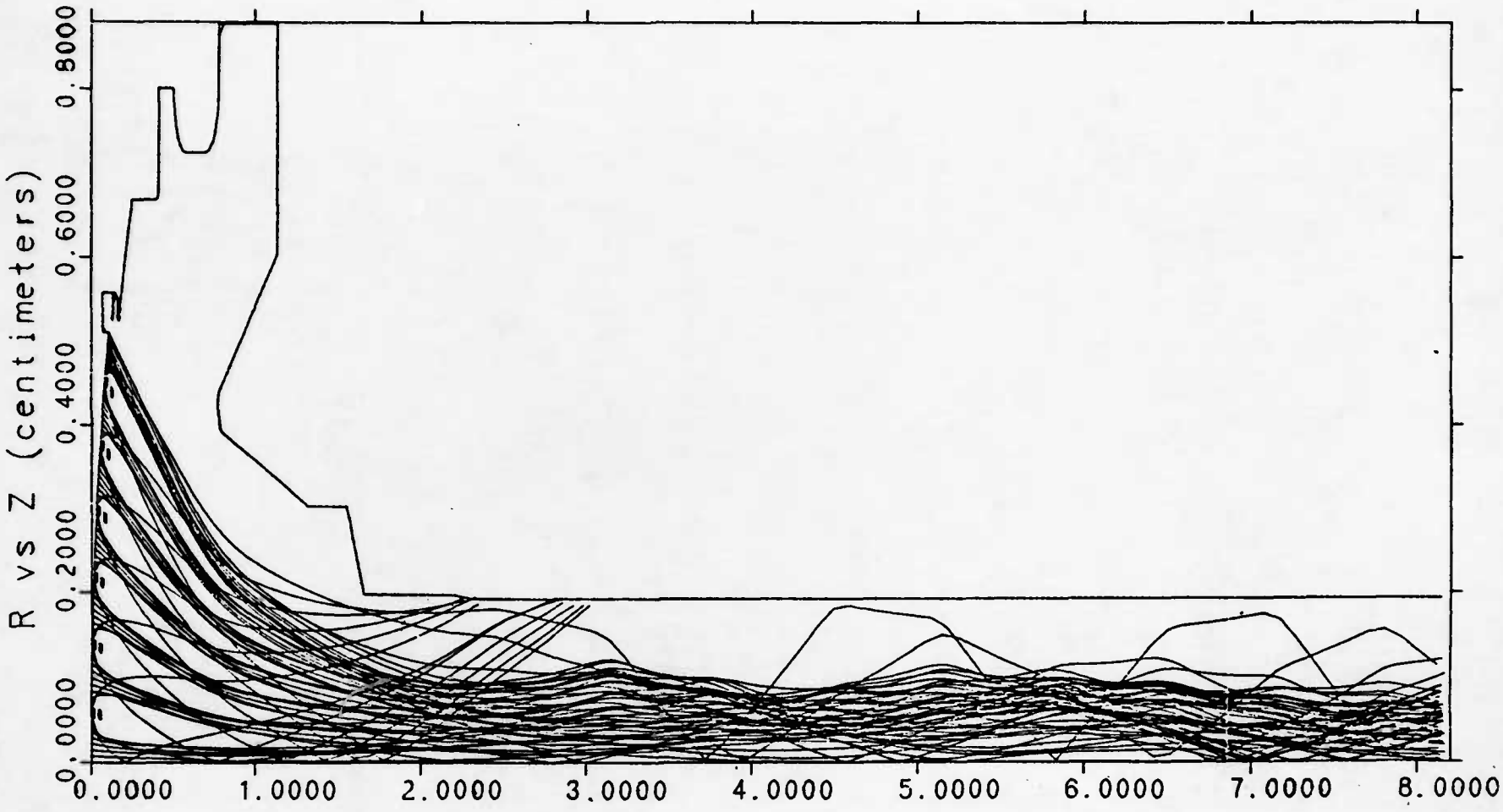

(a) Gun region.

Fig. 36. Electron trajectories using the new method to verify tunnel emittance growth.

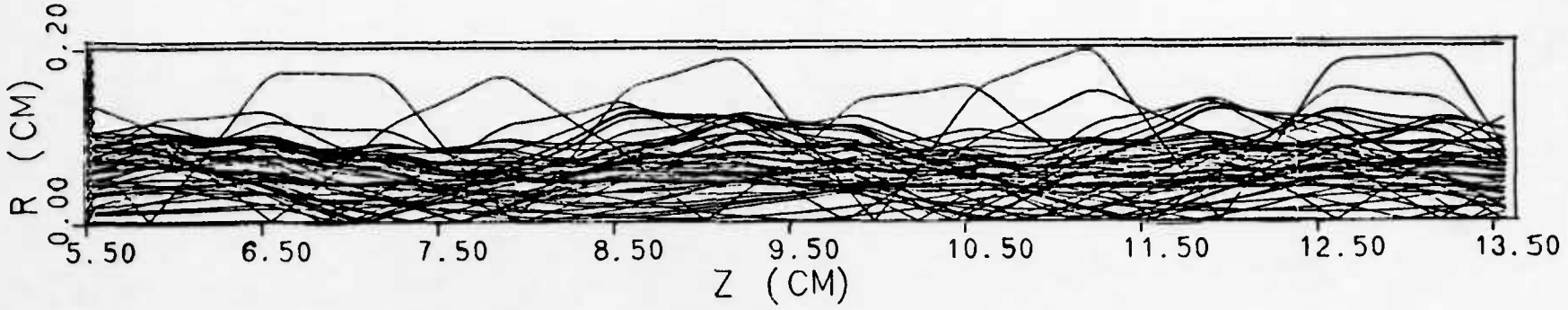

(b) First continuation.

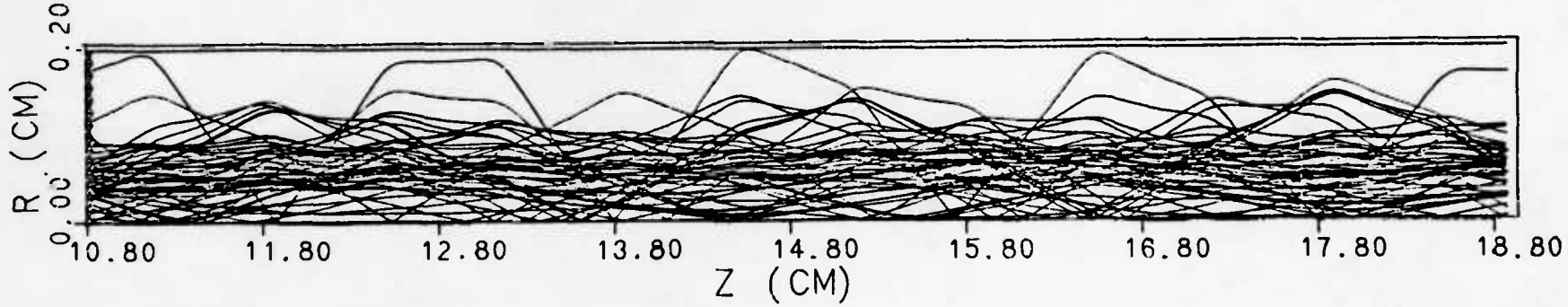

(c) Second continuation.

Fig. 36. Continued.

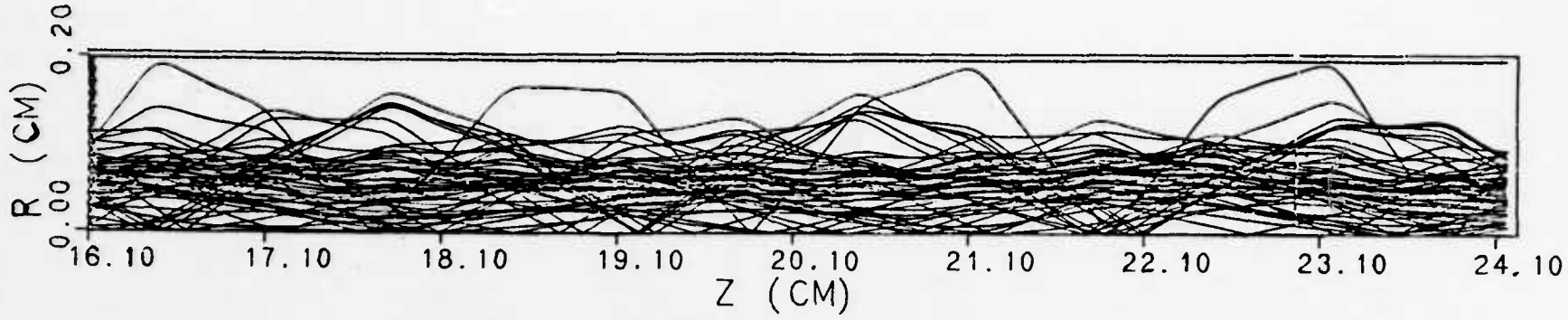

(d) Third continuation.

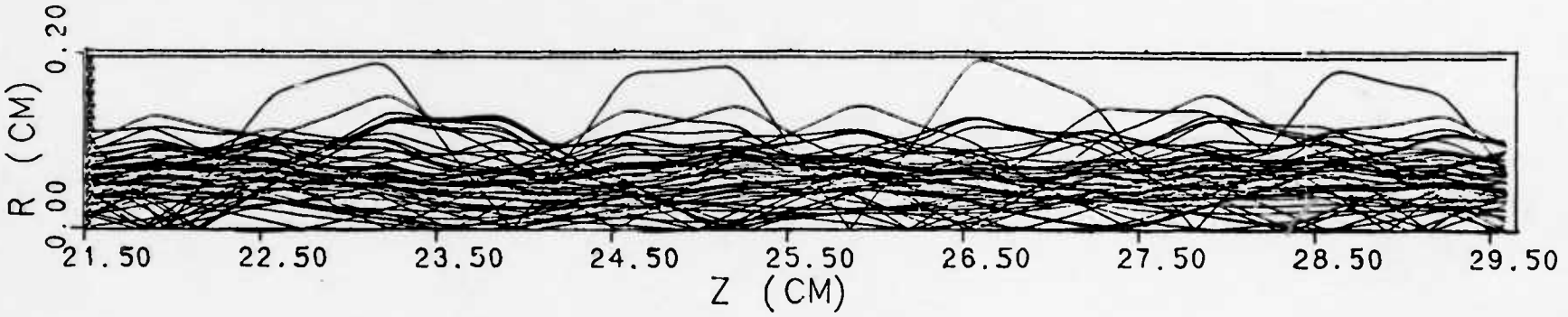

(e) Fourth continuation.

Fig. 36. Continued.

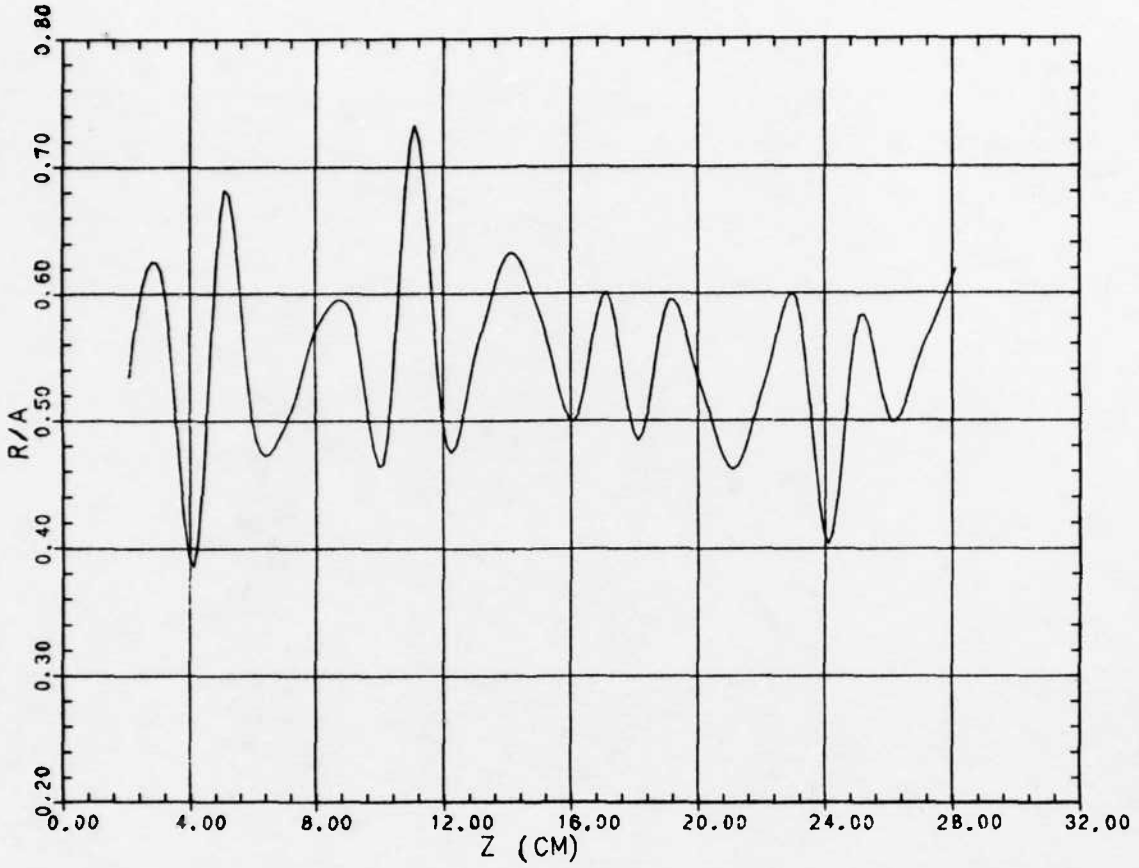

Fig. 37. Beam filling factor versus axial distance for beam profile of Fig. 36.

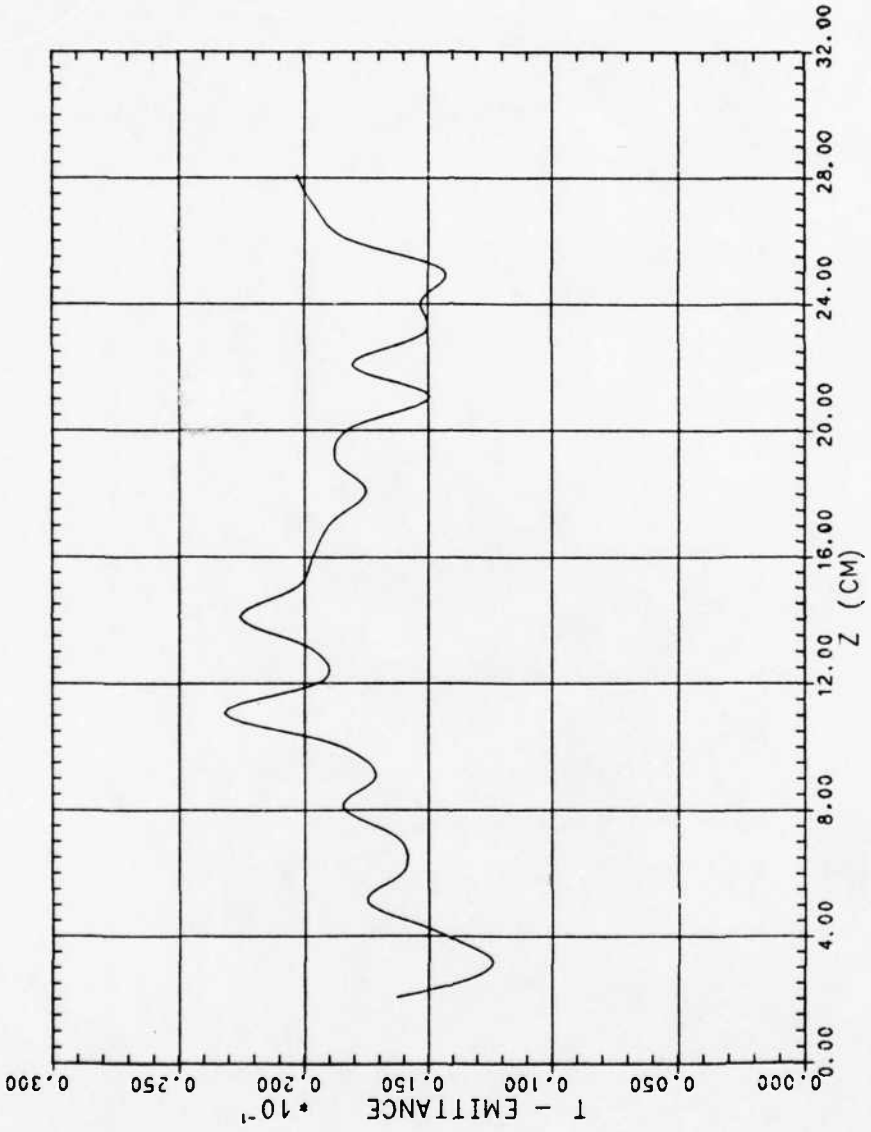

Fig. 38. T-emittance versus axial distance for beam profile of Fig. 36.

Table 3. R95/A values obtained from the beam of Fig. 36.

Z(cm)	R95/A				
	(a)	(b)	(c)	(d)	(e)
2.1	0.53012				
3.1	0.61764				
4.1	0.38485				
5.1	0.68209				
6.1	0.48430	0.48494			
7.1	0.49350	0.49939			
8.1	0.62570	0.57645			
9.1		0.58652			
10.1		0.46522			
11.1		0.73263	0.73248		
12.1		0.48014	0.48044		
13.1		0.56792	0.56086		
14.1			0.63224		
15.1			0.57719		
16.1			0.49879		
17.1			0.60281	0.60074	
18.1			0.48126	0.48393	
19.1				0.59511	
20.1				0.52649	
21.1				0.46100	
22.1				0.52809	0.52801
23.1				0.59543	0.59591
24.1				0.41422	0.40302
25.1					0.58199
26.1					0.49863
27.1					0.55821
28.1					0.61933
29.1					0.52938

Table 4. T-emittance values obtained from the beam of Fig. 36.

Z(cm)	T-Emittance				
	(a)	(b)	(c)	(d)	(e)
2.1	0.01633				
3.1	0.01240				
4.1	0.01445				
5.1	0.01750				
6.1	0.01620	0.01597			
7.1	0.01620	0.01621			
8.1	0.02060	0.01846			
9.1		0.01714			
10.1		0.01876			
11.1		0.02319	0.02320		
12.1		0.01932	0.01928		
13.1		0.01992	0.01969		
14.1			0.02256		
15.1			0.02024		
16.1			0.01963		
17.1			0.01881	0.01896	
18.1			0.01566	0.01753	
19.1				0.01880	
20.1				0.01817	
21.1				0.01494	
22.1				0.01815	0.01811
23.1				0.01523	0.01514
24.1				0.01558	0.01530
25.1					0.01439
26.1					0.01836
27.1					0.01961
28.1					0.02013
29.1					0.01788

The plot of the beam filling factor over the full length of the tube shows the average size of the beam remaining fairly constant. Tunnel emittance is shown increasing from a minimum value of 0.012 to a maximum value of 0.023. Since this was a nonthermal simulation, corrections will still have to be made to be able to compare these values to that predicted by Eq. 8 in reference 2.

Figure 37 also shows tunnel emittance exhibiting a wavelike behavior. After growing to a maximum of about 0.023, tunnel emittance proceeded to decay to a value of approximately 0.014. It then started growing again until it reached a value of approximately 0.021 at the end of the tube. If tunnel emittance is indeed growing and decaying in a cycle, this could be a very significant discovery. This implies that tubes could be designed such that the dc beam will have minimum tunnel emittance at the end of the tube. This will result in an additional increase in beam transmission and high tube efficiency.

It is noteworthy to point out that tunnel emittance did not decay to its minimum value. After reaching its first maximum, it decayed to a value of approximately 0.014. Even if it is truly cycling, it seems that it does not return back to its initial value.

B. Suggestions for Further Study

We have now predicted emittance growth over the full length of a tube. The simulation that was made resulted in several interesting results that need experimental verification. The next step before embarking on any experimental measurements is to extend the simulation until determination of the wave-like behavior could be made. Also,

perturbations in the entrance condition could be introduced to determine how these will affect tunnel emittance. In particular, the position of the beam waist with respect to the entrance magnetic field could be varied to determine if there is an optimum position that will result in minimum emittance growth and higher beam transmission. The effects of shunting the magnetic field could also be simulated by varying magnetic field values along the tube. Adjustments of the B-field could be made at the locations of the beam excursions in Fig. 36 to observe the effects of this process.

To determine the accuracy of this new beam segmentation method, the 5637 gun and the 5638 body could be put together and tested in the gun analyzer. A thermal simulation using this new method has to be made so that accurate comparison between measured and predicted values could be made. Once accuracy and reliability of this new method is established, a tube could be built to verify experimentally the predicted emittance growth.

C. Final Remarks

In addition to the development of a new method of ray tracing for emittance growth studies in very long beams, the work uncovered what appears to be a fundamental problem in all codes which use a paraxial approximation for space-charge (see Section IV.B). The implication is that codes employing such paraxial approximation will have inherent errors in the solution. This can be verified by comparing the results of paraxial based codes to nonparaxial results from DEMEOS.

REFERENCES

1. R. True, "Tunnel Emittance Growth in PPM Focused TWT's," IEDM Technical Digest, December 1985, pp. 192-195.

2. R. True, "Emittance and the Design of Beam Formation, Transport, and Collection Systems in Periodically Focused TWT's," IEEE Transactions on Electron Devices, Vol. ED-34, No. 2, February 1987.

3. R. True, "The Deformable Relaxation Mesh Technique for Solution of Electron Optics Problems," IEDM Technical Digest, December 1975, pp. 257-260.

4. R. True, "Control of Emittance Growth in PPM Focused TWT's," Proceedings of the IEDM, December 1986.

5. R. True, "Gridded Pierce Gun Design and the PPM Focusing of Beams from Gridded Electron Guns," IEDM Technical Digest, December 1982, pp. 32-35.

6. R. True, "A Theory for Coupling Gridded Gun Design with PPM Focusing," IEEE Transactions on Electron Devices, Vol. ED-31, No. 3, March 1984, pp. 353-362.

7. J. Hechtel, "Analysis of Non-Laminar Electron Beams for High-Power Microwave Electron Tubes," IEDM Technical Digest, 1974, pp. 197-200.

8. K. H. Krause, A Dynamic Refocusing System for Designing Charged Particle Beam Microwave Tubes, Degree of Engineer Thesis, Stanford University, Stanford, California, May 1977.

MISSION
of
Rome Air Development Center

RADC plans and executes research, development, test and selected acquisition programs in support of Command, Control, Communications and Intelligence (C^3I) activities. Technical and engineering support within areas of competence is provided to ESD Program Offices (POs) and other ESD elements to perform effective acquisition of C^3I systems. The areas of technical competence include communications, command and control, battle management, information processing, surveillance sensors, intelligence data collection and handling, solid state sciences, electromagnetics, and propagation, and electronic, maintainability, and compatibility.

DTIC

4-89

END

DATE

FILMED